Summer 2024

Machine Learning Based Three-Limb Core-Type Transformer Core Aspect Ratios Identification

Ananta Bijoy Bhadra

Recommended Citation

Bhadra, Ananta Bijoy, "Machine Learning Based Three-Limb Core-Type Transformer Core Aspect Ratios Identification" (2024). *Electronic Theses and Dissertations*. 2803.
https://digitalcommons.georgiasouthern.edu/etd/2803

MACHINE LEARNING BASED THREE-LIMB CORE-TYPE TRANSFORMER CORE ASPECT RATIOS IDENTIFICATION

by

ANANTA BIJOY BHADRA

(Under the Direction of Reza Jalilzadeh Hamidi)

ABSTRACT

Power transformers are considered one of the key elements of electric grids. Transient studies include transformer transient analysis which is required for the continuous power supply. However, to perform the transient analysis, the details of the internal structure of the transformer are required which are unobtainable and considered as confidential information. Therefore, the application of topological-based transformer models is limited although the models can accurately represent the transformers. To address this concern, a novel approach utilizing Machine Learning (ML) to identify the core aspect ratios of the three-limb core-type transformer is introduced. The proposed approach, using only the voltage and current measurements in the steady-state, no-load condition, employs the Extreme Gradient boosting (XGBoost) algorithm to identify the core aspect ratios. MATLAB/Simscape is used to model transformers. The results illustrate that the proposed algorithm is able to identify the core aspect ratios correctly.

INDEX WORDS: Extreme Gradient Boosting (XGBoost), Transformer core aspect ratios, Parameter identification, Unified magnetic Equivalent Circuit (UMEC).

MACHINE LEARNING BASED THREE-LIMB CORE-TYPE TRANSFORMER CORE ASPECT RATIOS IDENTIFICATION

by

ANANTA BIJOY BHADRA

B.S., Rajshahi University of Engineering & Technology, 2019

A Dissertation Submitted to the Graduate Faculty of Georgia Southern University
in Partial Fulfillment of the Requirements for the Degree

MASTER OF SCIENCE

ALLEN E PAULSON COLLEGE OF ENGINEERING AND COMPUTING

STATESBORO, GEORGIA

MACHINE LEARNING BASED THREE-LIMB CORE-TYPE TRANSFORMER CORE ASPECT RATIOS IDENTIFICATION

by

ANANTA BIJOY BHADRA

Major Professor: Reza Jalilzadeh Hamidi

Committee: Fernando Rios

Mohammad Ahad

Electronic Version Approved:

July 2024

DEDICATION

I would like to pay tribute to my parents and my younger brother for my achievements. They were constantly supporting me in every situation and decision of my life. Without their unwavering belief in me, I would not be able to complete the project. Their encouragement derived me throughout my life. I also owe a debt to my friends, lab mates and roommates who provided steady support and suggestions which were an essential part of the journey.

ACKNOWLEDGMENTS

I would like to express my gratitude to Dr. Reza Hamidi, who has been an exceptional mentor and guide throughout the degree. Without his suggestions and mentorship, it was not possible for me to pursue my master’s degree. I am grateful to him for his trust, support, encouragement, and guidance during the project. Moreover, I would like to thank my thesis committee members, Dr. Fernando Rios and Dr. Mohammad Ahad, for their valuable insight and constructive suggestions. I would also like to thank Ms. Tiffany Courdin for her assistance with the administrative tasks associated with my assistantship position. I am also grateful to Dr. Haddad for his guidance and inspiration throughout my studies. The university provided me with a platform of personal and academic growth for two and a half years. Hence, I would also like to extend my gratitude to the university community for their support and contribution.

TABLE OF CONTENTS

Page

CHAPTER

LIST OF TABLES

LIST OF FIGURES

Page

CHAPTER 1

INTRODUCTION

Power transformers are considered as the fundamental elements of the power delivery system. Transformers transients possess significant impact on electric grids(“IEEE Draft Guide to Describe the Occurrence and Mitigation of Switching Transients Induced by Transformers, Switching Device, and System Interaction,” 2022). For this reason, study of transformer transients is essential. To ensure the proper analysis of the transients, accurate transformer modelling is required. This modelling involves requirement of certain transformer parameters which are often unavailable and considered as proprietary information by the manufacturers (Dick & Watson, 1981; Yang et al., 2018). To address this issue, different transformer models have been established by the researcher. These models involve different theorems (e.g., duality) to establish the accurate transformer model. These models require different parameters, and these parameters are achievable to some extent. These models are categorized into two major groups as non-topological and topological transformer models. However, the issue of accurate transformer modelling has been a major concern for the researchers. The use of actual transformer parameters results in the most accurate transformer modelling. As discussed before, these parameters are generally unavailable.

The purpose of this dissertation project is to identify the core aspect ratio parameters of the three-limb core-type transformers. The aspect ratio parameters indicate the actual core size of a transformer which is retained by the manufacturer.

Chapter 2 provides an overview on non-topological transformer modelling and the results of the literature search. It also provides the application of these transformer models used for the transient simulation.

Chapter 3 describes the topological transformer models and their application. It also explains the use and advantages of topological modelling over non-topological models and the selection of the transformer model for parameter identification.

Chapter 4 demonstrates different approaches of parameter identification based on the transformer models explained in Chapter 2 and Chapter 3. It also illustrates the limitations of the existing approaches.

Chapter 5 explains the proposed algorithm to identify the core aspect ratio parameters. It also demonstrates the other approaches taken during the project for the identification of purpose and their limitation in identifying the core aspect ratios.

Chapter 6 demonstrates the effectiveness of the proposed algorithm through test cases. An illustrative test case is provided to explain the algorithm along with the process of identifying the transformer core aspect ratios.

Chapter 7 contains the summary and conclusion of the project. It also provides the scope of future works and improvements which can be a starting point for other research projects in this area of research.

CHAPTER 2

NON-TOPOLOGICAL TRANSFORMER MODELS

2.1 STC Model

The transformer models are classified into two categories. These are: topological and non-topological. The non-topological models are defined as transformer models established based on the equivalent parameters rather than physical information. These parameters can be both electrical and magnetic parameters. These transformer model parameters are found both from the manufacturer and different tests performed. One of the transformer models is named as Saturable Transformer Component (STC) model. It is also known as the nameplate transformer (*EMTP-RV.*, n.d.). The STC transformer is based on the Steinmetz model (Steinmetz, & Berg, 1900). This model has been considered as one of the fundamental and established transformer models. This model uses electrical parameters such as resistors and capacitors to model a transformer. Figure 1 demonstrates the single-phase STC transformer model.

In the Figure 1 (a), V_P is the primary side voltage of the transformer, L_P and R_P denotes the primary side inductance and resistance of the transformer, R_M denotes the core loss of the transformer, L_M is the core flux of the transformer, N_P and N_S are the number of primary and secondary side turns respectively, L_S and R_S indicates the secondary side inductance and resistance of the transformer, and V_S is the secondary-side voltage of the transformer. STC model is one of the fundamental and simple transformer models. However, this model has several limitations. This model is not able to represent the inter-phase mutualities, Due to this, the three-phase transformers can be modelled only by the three-phase transformer

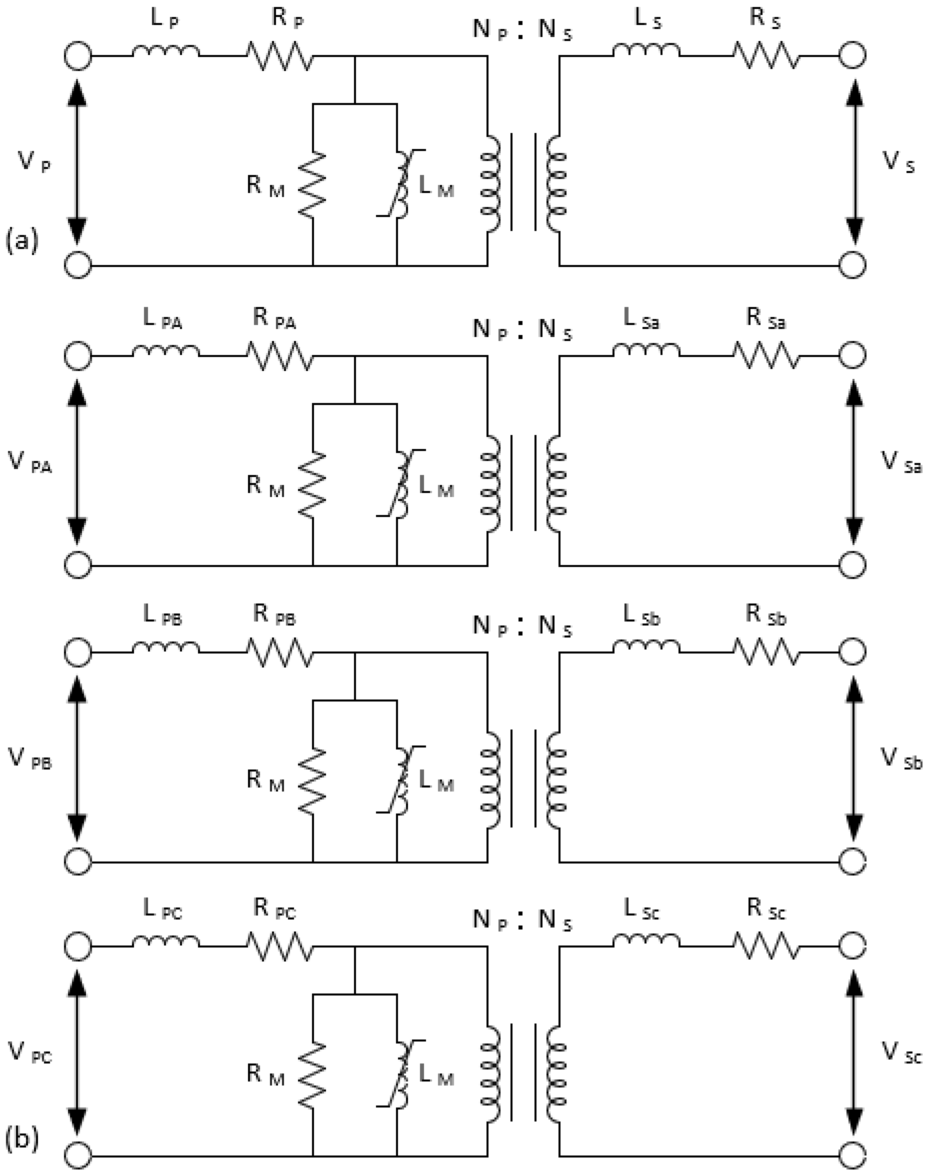

Figure 1. STC transformer model (Martinez-Velasco, 2011).

banks. Moreover, it cannot differentiate between positive- and zero-sequence impedances. Therefore, the application of this transformer is limited (Hamidi, 2023; Jazebi & De Leon, 2015).

2.2 BCTRAN Model

Another non-topological transformer model is the BCTRAN model. It is introduced to address the issues of the STC model (Brandwajn et al., 1982). This model uses the nameplate and short-circuit and open-circuit test data to identify the required parameters of the transformer. Using this model, the issue of inter-phase mutualites is solved as this model uses both self- and mutual- inductances to model the transformer. Moreover, the three-phase transformer can be modelled in the form of branch impedance and resistance matrix. This model. Moreover, this model can be used for M number of windings. Figure 2 shows the BCTRAN model representation of P-phase M-winding transformer.

In the BCTRAN model, based on the nameplate and test data, an inductance matrix, $\boldsymbol{L}$ along with resistance matrix, $\boldsymbol{R}$ is calculated. The issue of inverting singular $\boldsymbol{L}$ is avoided by creating $\boldsymbol{AR}$ model where $\boldsymbol{A}$ is the inverse of $\boldsymbol{L}$. The $\boldsymbol{L}$ contains both self- and mutual-inductances. The transformer is modelled as (Cho, 2002),

$$\begin{bmatrix} V_1 \\ V_2 \\ \vdots \\ V_N \end{bmatrix} = \begin{bmatrix} R_{11} & 0 & \cdots & 0 \\ 0 & R_{22} & \cdots & 0 \\ \vdots & \vdots & \ddots & \vdots \\ 0 & 0 & \cdots & R_{NN} \end{bmatrix} \begin{bmatrix} I_1 \\ I_2 \\ \vdots \\ I_N \end{bmatrix} + \begin{bmatrix} L_{11} & L_{12} & \cdots & L_{1N} \\ L_{12} & L_{22} & \cdots & L_{2N} \\ \vdots & \vdots & \ddots & \vdots \\ L_{N1} & L_{N2} & \cdots & L_{NN} \end{bmatrix} \frac{d}{dt} \begin{bmatrix} I_1 \\ I_2 \\ \vdots \\ I_N \end{bmatrix} \tag{1}$$

$$\boldsymbol{L}^{-1}.\boldsymbol{V} = \boldsymbol{L}^{-1}.\boldsymbol{R}.\boldsymbol{I} + \frac{d}{dt}\boldsymbol{I} \tag{2}$$

where, $\boldsymbol{V}$ is the vector of terminal voltages and $\boldsymbol{I}$ is the vector of currents. As this model is able to resolve the issue of the inter-phase mutualities, the accuracy of BCTRAN model in transformer modelling is notable. However, the BCTRAN model has issues regarding accurate transformer modelling. Although it is more accurate than the STC model, The BCTRAN model does not represents the core non-linearity and losses. As a result, the model requires external attachment of nonlinear core elements to model the core. The nonlinear core elements are represented by external nonlinear inductors and a network of resistors

(Alvarez-Marino et al., 2012). This improvement is named as BCTRAN+ model is some cases. (Ang, 2010; PENG, 2013). However, the BCTRAN+ model is not irreversible (Yang et al., 2018). Moreover, the BCTRAN model is only accurate for the frequencies below 1 KHz (Martinez et al., 2005; Martinez & Mork, 2005).

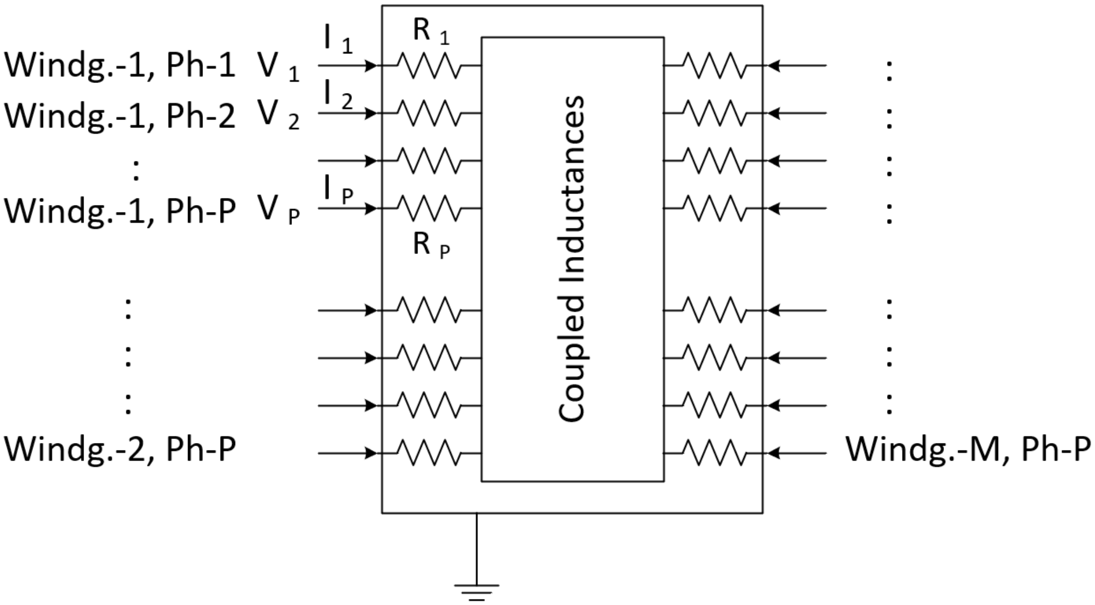

Figure 2. BCTRAN model (Cho, 2002).

Overall although the non-topological models are simple in nature, transformers require general information such as nameplate and test data to model a transformer, the accuracy of the modelled transformer is fundamental issue for this type of transformers. Considering this issue, the topological models are introduced. Table 1 shows the comparison between the STC and BCTRAN model. The comparison indicates that BCTRAN has advantages over the STC model as it is applicable easily for the three-phase transformer considering the mutuality. Moreover, the BCTRAN model is irreversible in nature and general available test data is used to model the transformer.

Table 1. Comparison between STC and BCTRAN model

Transformer Type Characteristics	STC	BCTRAN
Design Parameters	Leakage inductances and winding resistances	Self and mutual inductances and resistances
Data available	Yes	Yes
Irreversible	N/A	Yes
Sequence	No	Yes

CHAPTER 3

TOPOLOGICAL TRANSFORMER MODELS

3.1 Duality-based Model

The topological models are defined as transformer models established based on the physical information of the transformer. These models are more accurate in transformer modelling as they use real dimensional parameters rather than equivalent parameters. One of the topological models is the duality-based model. This model is proposed based on the principle of duality (Cherry, 1949). This model involves the saturation effect on the transformer which was absent in the non-topological models. In the duality-based model, the transformer is modelled as a magnetic equivalent circuit rather than an electric equivalent circuit. Table 2 shows the elements of magnetic and electric equivalent circuits (Cho, 2002).

Table 2. Equivalent Magnetic and Electric for Duality Transformation

Electric Circuit Elements	Magnetic Circuit Elements
Voltage (V)	$\frac{d\lambda}{dt}$
Current (I)	MMF
Inductance (L)	Reluctance ($\mathcal{R}$)

The relation between magnetic and electric circuit is established as,

$$\begin{cases} V = \dfrac{d\lambda}{dt} \\ MMF = Ni \\ L = \dfrac{N^2}{\mathcal{R}} \end{cases} \tag{3}$$

$$\mathcal{R} = \frac{l}{\mu A} \tag{4}$$

where l is the length of the section and A is the area of the cross-section. Using (3) and (4), a three-phase three-limb transformer model is shown in Figure 3.

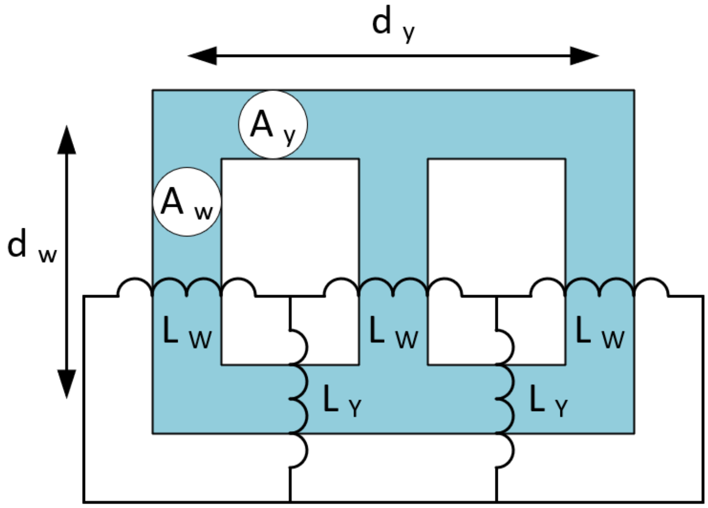

Figure 3. Duality-based model with actual core (Shafieipour et al., 2019).

The inductances of the duality-based transformer model are,

$$\begin{cases} L_W = \dfrac{N^2.\,\mu.\,A_w}{d_w} \\ L_Y = \dfrac{N^2.\,\mu.\,A_y}{d_y} \end{cases} \tag{5}$$

The duality derived models are more accurate since they use the core dimensions to estimate the magnetic parameters. These models can be implemented not only as ideal transformer, but also as saturable inductor and lumped RLC.

However, the practical application of the duality-based models is limited as the ore dimensions are not generally available. Moreover, the factory test data is not enough to find the parameters of the duality-based models.

3.2 Unified Magnetic Equivalent Circuit (UMEC) model

Another topological model is the UMEC model. The UMEC model is closely related to the duality-based model. A general representation of the UMEC model is shown in Figure. 4. The UMEC model involves not only the core representing inductances, but also the leakage inductances. The advantage of UMEC is it is able to represent the transformer core along with the inter-phase mutualities. Therefore, overall, the topological models are more accurate than the non-topological models.

Based on the literature discussed above, the UMEC model is considered as one of the best transformers representing model. This model uses the duality principle to resolve the issue of core representation. Moreover, the reluctances are based on the core dimensions which yields more accurate modelling.

As the UMEC model is more accurate compared to all topological and non-topological models, this study uses the UMEC transformer modelling. The formulation for the UMEC model is also provided since the UMEC model is modified for this project to mitigate the computational burden. After that, the state-representation of transformer model is also developed. Figure 4(a) and (b) depicts the core structure of the three-limb transformer and the magnetic circuit model of the transformer. In this study, the core of the three-limb transformer is studied.

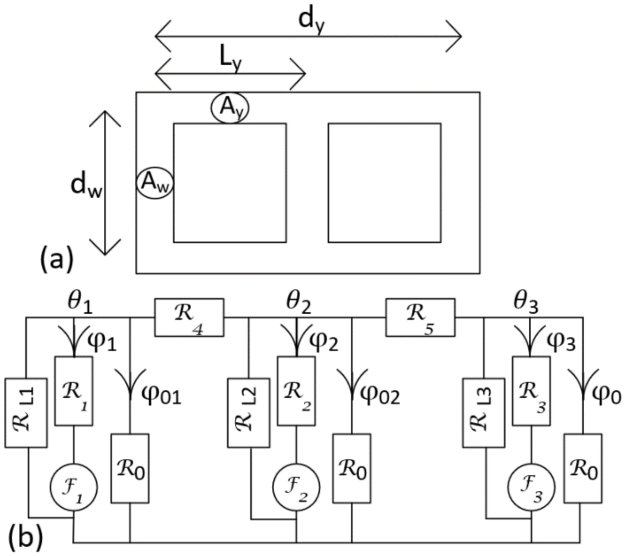

Figure 4. (a) Core of the three-limb transformer, (b) Equivalent magnetic model of the three-limb transformer

3.3 Modified UMEC Model

The formulation of the UMEC model has been established (W. G. Enright et al., 1999). However, the formulation of the UMEC model has been modified in this project. The formulation of the UMEC model is established for the no-load situation of the practical transformers. This formulation not only conserves the accuracy of the model but also reduces the computational complexity of the model. As the model is simple in terms of computation, large dataset can be developed for the Artificial Intelligence (AI) method used in this project. Figure. 4(b) indicates the equivalent magnetic circuit of the transformer on no-load condition. It is to note that, since the transformer is energized from one-side, the magnetomotive force (f) of the open-side is removed (W. G. Enright et al., 1999). The reluctances of the limb and yoke are based on the physical dimensions of the core ($R = \frac{L}{\mu_0 \mu_r A}$) where L is the effective length of the core segment and A is the cross-section of the core segment. Hence, four dimensions are required to model the three-limb transformers. These are: the effective length of the yoke, ($L_y = d_y/2$), effective length of the limb section, (L_w), cross-section area of the yoke, (A_y) and the cross-section area of the limb (A_w). Based on the dimension, the following ratios are established (W. G. Enright et al., 1999),

$$\begin{cases} r_{lyw} = \dfrac{d_y}{d_w} \\ r_{ayw} = \dfrac{A_y}{A_w} \end{cases} \tag{6}$$

where r_{lyw} is the ratio of the yoke length to limb length and r_{ayw} is the ratio of the yoke cross-section to limb cross-section. The core is considered as symmetrical in structure for the practical transformers and hence the limb reluctances ($R_1 = R_2 = R_3 = \frac{d_w}{\mu_0 \mu_r A_w}$), yoke reluctances ($R_4 = R_5 = \frac{d_y/2}{\mu_0 \mu_r A_y}$), and air reluctances ($R_0$) are same (Xusheng, 1996). As the

L_w and A_w are considered as the base for normalization, the permeances of the limbs (P_L) and yokes (P_Y) are calculated as:

$$\begin{cases} P_L = \dfrac{\mu_0\mu_r A_w/A_w}{d_w/d_w} = \mu_0\mu_r \\ P_Y = \dfrac{\mu_0\mu_r A_y/A_w}{d_y/(2L_w)} = \dfrac{2\mu_0\mu_r r_{ayw}}{r_{lyw}} \end{cases} \tag{7}$$

The air permeance (P_0) is found from the zero-sequence short-circuit test result when the core is not saturated (Xusheng, 1996).P_0 is defined as, $P_0 = \omega X_{st_0}/V^2$ where ω is the angular frequency, X_{st_0} is the zero-sequence short-circuit reactance and V is the nominal voltage of the winding of the transformer. Based on the Figure. 4(b), the nodal analysis of the transformer can be written as,

$$\begin{cases} P_{L1}\theta_1 + \phi_1 + \phi_{01} + P_Y(\theta_1 - \theta_2) = 0 \\ P_{L2}\theta_2 + \phi_2 + \phi_{02} - P_Y(\theta_1 - 2\theta_2 + \theta_3) = 0 \\ P_{L3}\theta_3 + \phi_3 + \phi_{03} + P_Y(\theta_3 - \theta_2) = 0 \end{cases} \tag{8}$$

where θ is the nodal mmf. Considering, $\phi_{01} = P_0\theta_1$, $\phi_{02} = P_0\theta_2$, and $\phi_{03} = P_0\theta_3$, (8) is written as (Xusheng, 1996),

$$\boldsymbol{\Phi} = \boldsymbol{P}\,\boldsymbol{\Theta} \tag{9}$$

where $\boldsymbol{\Phi} = [\phi_1, \phi_2, \phi_3]^{\mathrm{T}}$, $\boldsymbol{\Theta} = [\theta_1, \theta_2, \theta_3]^{\mathrm{T}}$, and

$$\boldsymbol{P} = \begin{bmatrix} a & P_Y & 0 \\ P_Y & b & P_Y \\ 0 & P_Y & c \end{bmatrix}$$

where $a = -(P_{L1} + P_0 + P_Y)$, $b = -(P_{L2} + P_0 + 2P_Y)$, and $c = -(P_{L3} + P_0 + P_Y)$. Moreover,

$$\begin{cases} \phi_1 = P_L(\theta_1 - N_1 i_1) \\ \phi_2 = P_L(\theta_2 - N_2 i_2) \\ \phi_3 = P_L(\theta_3 - N_3 i_3) \end{cases} \tag{10}$$

where for practical transformers, $N_1 = N_2 = N_3$. Hence, the matrix formulation is found as,

$$\boldsymbol{\Phi} = P_L\boldsymbol{\Theta} - N\boldsymbol{i} \tag{11}$$

where $\boldsymbol{i} = [i_1, i_2, i_3]^T$ and i_1, i_2, and i_3 are winding currents. Using (9) in (11), the equation of mmf is found as,

$$\boldsymbol{\Phi} = P_L\boldsymbol{P}^{-1}\boldsymbol{\Phi} - N\boldsymbol{i} \tag{12}$$

and,

$$(P_L\boldsymbol{P^{-1}} - \boldsymbol{I})\boldsymbol{\Phi} = N\boldsymbol{i}. \tag{13}$$

Moreover, it is found that, $\frac{N_1}{N_2} = \frac{V_1}{V_2}$ where V is the terminal voltage of the energized windings. (W. G. Enright et al., 1999). Hence,

$$\boldsymbol{\Phi} = (P_L\boldsymbol{P^{-1}} - \boldsymbol{I})^{-1}V\boldsymbol{i}. \tag{14}$$

Based on the discussion above, the inductance matrix is found as,

$$\boldsymbol{L} = (P_L\boldsymbol{P^{-1}} - \boldsymbol{I})^{-1}V. \tag{15}$$

The formulated equation reduces the computational complexity of this model and reduces the runtime of the simulation for dataset generation.

3.4 State-Space Representation of The UMEC Model

Transformer dynamics are discussed in this section. First, Figure 5 is considered to represent the circuit model of the three-limb transformer. The winding resistors are added to the model in series with the windings. Based on this, the flux linkage derivative ($\dot{\lambda}$) is found as (Kazemi et al., 2021),

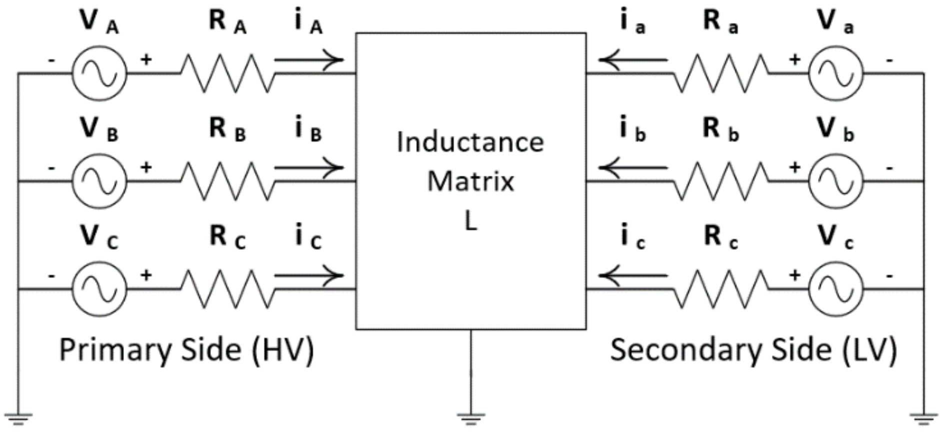

Figure 5. Circuit Model of the transformer (Kazemi et al., 2021).

$$\begin{cases} \dot{\lambda_A} = V_A - R_A i_A \\ \dot{\lambda_B} = V_B - R_B i_B \\ \dot{\lambda_C} = V_C - R_C i_C \\ \dot{\lambda_a} = V_a - R_a i_a \\ \dot{\lambda_b} = V_b - R_b i_b \\ \dot{\lambda_c} = V_c - R_c i_c \end{cases} \tag{16}$$

where V_A, V_B, and V_C are the voltages of the primary side windings and V_a, V_b, and V_c are the secondary-side winding voltages. i_A, i_B, and i_C are the primary side currents and i_a, i_b, and i_c are the secondary side currents. The matrix is formulated as,

$$\boldsymbol{\lambda}=\boldsymbol{V}-\boldsymbol{Ri} \tag{17}$$

where $\dot{\boldsymbol{\lambda}} = \left[\dot{\lambda_A}, \dot{\lambda_B}, \dots, \dot{\lambda_c}\right]^{\mathrm{T}}$ is the vector of the flux linkage derivatives, $\boldsymbol{V} = [V_A, V_B, \dots, V_c]^{\mathrm{T}}$ is the vector of winding voltages, $\boldsymbol{R} = \mathrm{diag}(R_A, R_B, \dots, R_c)$ is the resistance matrix, and $\boldsymbol{i} = [i_A, i_B, \dots, i_c]^{\mathrm{T}}$ is the vector of winding currents. The relation between the winding currents and total flux linkages are found as,

$$\boldsymbol{i} = \boldsymbol{\Gamma\lambda} \tag{18}$$

where $\boldsymbol{\Gamma} = \boldsymbol{L}^{-1}$. From the (17) and (18), the dynamic and observation equations in the state-space representation are found as (Kazemi et al., 2021; Xusheng, 1996),

$$\begin{cases} \dot{\boldsymbol{\lambda}} = \boldsymbol{A\lambda} + \boldsymbol{BV} \\ \boldsymbol{i} = \boldsymbol{\Gamma\lambda} \end{cases} \tag{19}$$

where $\boldsymbol{\lambda}$ is the state vector, $\boldsymbol{A} = -\boldsymbol{R\Gamma}$ is the state dynamic matrix, and $\boldsymbol{B} = \boldsymbol{I}$ is the input matrix ($\boldsymbol{I}$ is the identity matrix).

The discussed formulation of the UMEC model and the state-representation is used for transformer modelling and simulation. As the UMEC model is used, the aspect ratios are required to be found for the modelling of the transformer. The progress on finding different transformer parameters is elaborately discussed in the following chapter. Table 3 shows the difference between the duality and UMEC model.

Table 3. Comparison between Duality-based and UMEC model

Transformer Type Characteristics	Duality-based	UMEC
Design Parameters	Reluctances	Normalized or actual reluctances
Data available	No	No
Mutuality	Yes	Yes
Aspect ratios	No	Yes

CHAPTER 4

LITERATURE REVIEW ON PARAMETER IDENTIFICATION

As discussed earlier, the topological models are accurate but require actual or assumed core dimensions. The assumption of the core dimensions may lead to error in accuracy. Moreover, the nameplate data provided by the manufacturer may not be enough to find the transformer parameters. In this chapter, the progress on different transformer parameters identification is discussed. It explains the necessity of a system of identifying the transformer core aspect ratio parameters.

In (Jin et al., 2008), the authors proposed least-square method to identify the leakage inductances and winding resistances of the transformer. These parameters are identified through an improved orthogonal decomposition to reduce the numerical instabilities. However, the core parameters cannot be identified in this approach.

In (Calasan et al., 2020), to identify the parameters of the single-phase transformers, optimization techniques (i.e., the Manta Ray Foraging and Chaotic Manta Ray Foraging) are utilized. An objective function that receives transformers' no-load losses is also proposed to improve the accuracy of the method. However, the application of this method is limited to single-phase transformers.

In (Dirik et al., 2014), the winding resistances, leakage inductances, and core-loss-representing resistances are identified based on the Differential Equation Algorithm (DEA). The method uses real-time data to estimate these parameters and the parameters are identified while transformer remains in service.

In (Camelo-Daza et al., 2024), a nonlinear optimization problem is defined to identify the transformer parameters. After defining, the problem is solved by employing the Generalized Normal Distribution Optimizer (GNDO). However, this method is only applicable to the single-phase transformer model. There are plenty of works has been completed to identify the single-phase transformer parameters (Abdelwanis et al., 2020; Bhowmick et al., 2018; Illias et al., 2017; Mossad et al., 2014). However, these parameters are not applicable to identify the parameters of the three-phase transformers. Moreover, the inter-phase mutualities are also disregarded in these models.

There is not enough literature regarding the core parameters identification of the core-type three-limb transformers. In (Thilagar & Rao, 2002), the authors proposed parameter identification approach based on the Genetic Algorithm (GA). The parameter identification approach is to identify the three-phase STC transformer models which hase limited use in transient studies.

In (Brandwajn et al., 1982), the BCTRAN parameters are identified based on different conventional tests such as short-circuit and open-circuit tests. In (Narang & Brierley, 1994), the authors proposed a method where the outputs of conventional tests are translated to find the parameters required for the duality-based transformer models. Hence, this method is suitable for practical applications. However, zero-sequence short-circuit tests should be performed on the transformer with only one closed delta winding. Hence, it is one of the shortcomings of the proposed method. Furthermore, the inner and outer windings must concentrically and fully cover the limbs to the incorporation of the nonlinearities precisely. However, this is not possible for the practical transformers (McLyman, 2004).

In (Mork et al., 2007a, 2007b), to approximate the required parameters for the hybrid models, some tests are introduced. However, the tests require different combinations of short-circuited and open-circuited windings which may not be possible in practice.

In (X. Li et al., 2015), to identifying the nonlinear inductances incorporating the hysteresis characteristics, a method is proposed. This method is mainly suitable for UMEC-based transformer models. However, this method requires the use of core parameters such as core aspect ratios.

In addition to the discussed method, to identify the characteristics of transformers, several other literatures can be found. However, since the core dimensions are required for the finite element analysis, the application of these works are limited (Azzouz et al., 1993; Jazebi & De Leon, 2015; Srikanta Murthy et al., 2020).

Based on the discussion above, it is evident that the UMEC model is able to represent the transformer models accurately. However, due to the shortcomings in parameter identification for the UMEC models mentioned above, the application of the UMEC model in transient studies is limited.

In this project, addressing this issue, a novel Machine Learning (ML) method based on the Extreme Gradient Boosting (XGBoost) method with five-fold cross validation is proposed. The selection of the ML-based model is taken based on numerous attempts to employ the GA and Particle Swarm Optimization (PSO). In the next chapter, the proposed algorithm along with the different attempted methods and their limitations are discussed elaborately.

CHAPTER 5

PROPOSED ALGORITHM

5.1 Use of GA and PSO

After the selection of the transformer model, an algorithm is required to identify the core aspect ratios. This problem can be solved by using the general optimization algorithm such as GA and PSO. Attempts have been taken to employ the GA algorithm by testing it for different combinations of populations, generations, mutation ratios, crossovers, and elitism.

At first, two different simulation models are generated based on the UMEC model. One model works as the reference model while there other one is the model where the aspect ratios are required to be identified. Then, the following objective equation is proposed as,

$$F_{obj} = \sum_{Phase-A}^{Phase-C} \left(n\left(I_{ref(HV)} - I_{test(HV)}\right)\right)^2 + \sum_{Phase-a}^{Phase-c} \left(I_{ref(LV)} - I_{test(LV)}\right)^2 \qquad (20)$$

where $I_{ref(HV)}$ is the High Voltage (HV)-side current of the refence model, $I_{test(HV)}$ is the HV-side current of the test model of which the parameters are required to be identified, n is the ratio of number of turns in the transformer where $n > 1$, $I_{ref(LV)}$ is the Low Voltage (LV)-side current of the refence model, $I_{test(LV)}$ is the LV-side current of the test model of which the parameters are required to be identified. The value of objection function is expected to be close to 0 when both the models use the same aspect ratios. Figure. 6 shows an example of the objective function and inverse objective function (normalized) based on the change in aspect ratios. In this process, the GA algorithm is required to be applied and a minimum value of objective function is required to be set. Although the use of GA is simple, a universal minimum value of objective function applicable for all the transformers cannot be found. Hence, the use of GA did not yield a satisfactory result.

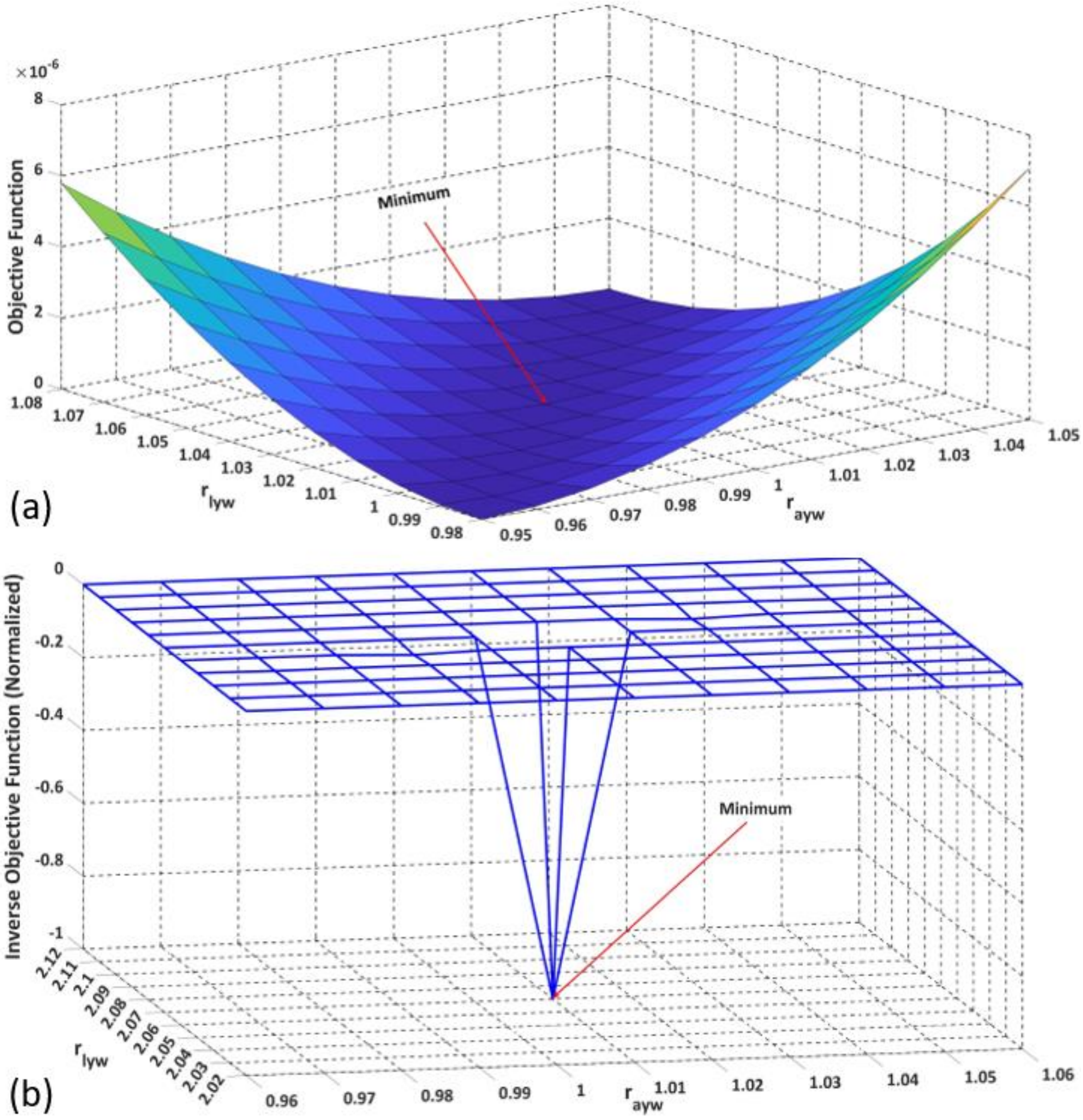

Figure 6. (a): Objective function with minimum value at different r_{lyw} and r_{ayw} of Tran-1, (b): Inverse objective function (normalized) with minimum value at different r_{lyw} and r_{ayw} of Tran-1.

For the PSO, extensive attempts were also made to identify the core aspect ratios. Similar to the GA, different parameters such as population sizes, inertia weights, cognitive parameters, velocity limits, and initialization methods are used. However, the PSO was not able to identify the ratios correctly. This leads to be use of the ML-based algorithm to identify the ratios correctly.

5.2 Use of ML

As the previous algorithms were unable to identify the ratios correctly, the ML-based algorithm is introduced. Figure 7 shows the flowchart to identify the core aspect ratios (r_{lyw} and r_{ayw}). The voltages and currents on the energized side are measured and recorded when the transformer is in no-load condition and its winding voltages and currents are in the steady state condition. They are named as v^{true} and i^{true} respectively.

To train the ML-based algorithm, a number of UMEC models of the transformer are made with a range of feasible core aspect ratios ($\hat{r}_{lyw}$ and $\hat{r}_{ayw}$) with small increments. The boundaries of these ratios are described in the later section named as "Selection of Feasibility Region".

After the selection of the range of the ratios, Each UMEC model with a pair of feasible ratios ($\hat{r}_{lyw}$ and $\hat{r}_{ayw}$) is simulated. The voltage for the simulation is the recorded voltage (v^{true}). As an example, if $1.2 \geq \hat{r}_{lyw} \geq 0.8$, then, the UMEC models are set up with $\hat{r}_{lyw} = 0.8, 0.805, 0.81, \ldots, 1.2$ while the recorded voltage v^{true} is supplied to each model to maintain the same simulation conditions.

For each test, the steady-state currents flowing into the transformer ($\hat{\imath}$) are measured and recorded until the entire feasible region is covered. To train and validate the proposed ML algorithm, the RMS values of $\hat{\imath}$'s and their harmonics as well as the feasible aspect ratios ($\hat{r}_{lyw}$ and $\hat{r}_{ayw}$) are used. This process is elaborated in in the later section named as "Proposed ML algorithm".

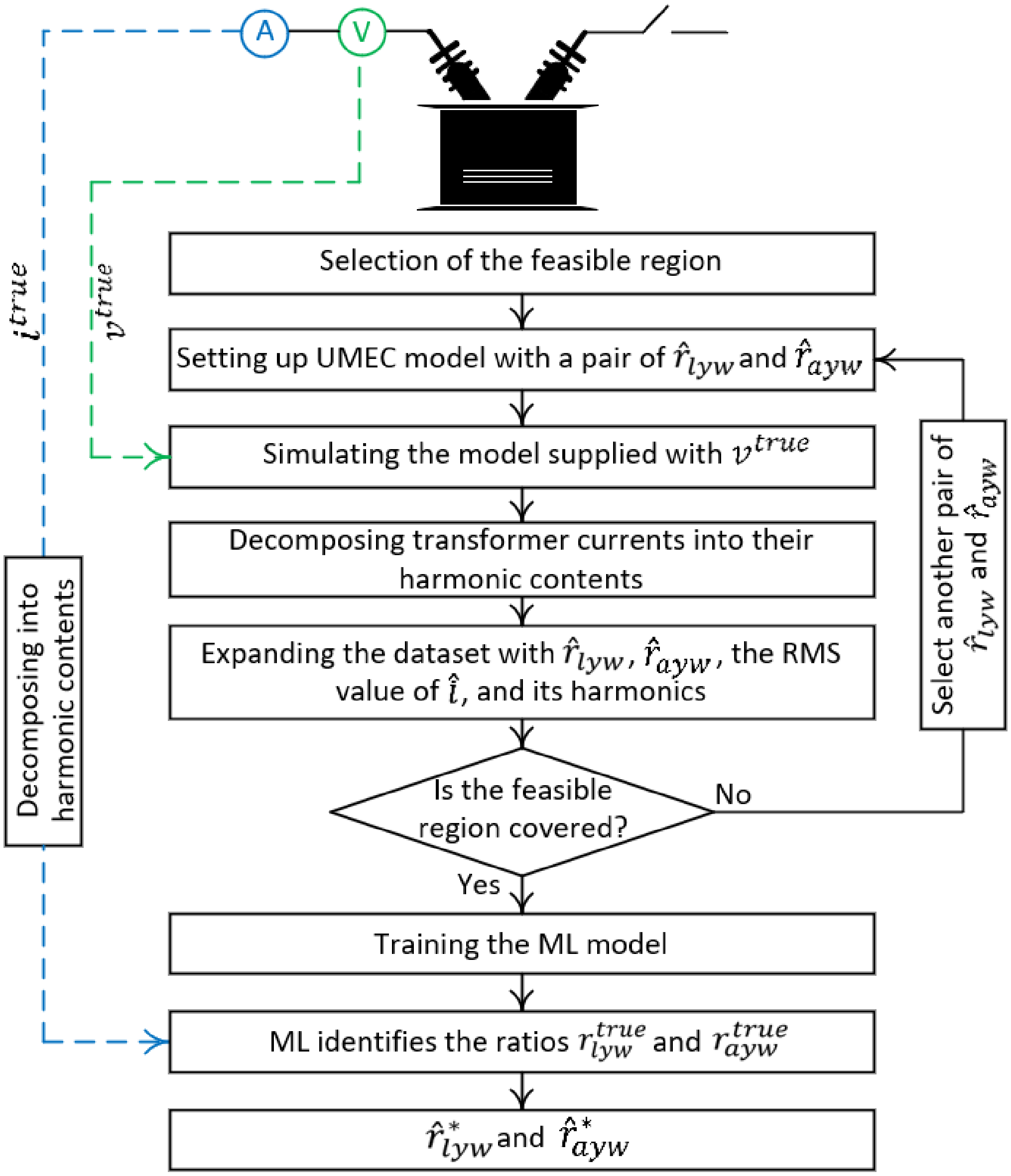

Figure 7. Flowchart of the proposed method.

5.3 Selection of Feasibility Region

As discussed earlier, a training set is required which is made by simulating the transformer using the UMEC. For this, a range of ratios are required. From Figure 4(a), it is evident that the yokes and limbs have the same amount of flux. Moreover, their cross-sections are close ($A_y \approx A_w$) in transformers. Hence, $r_{ayw} \cong 1$ (Shafieipour et al., 2020). To ensure that r_{ayw} is within a specific range, a margin of $\pm 20\%$ is introduced (Mitchell & Welsh, 2013). This leads to the r_{ayw} to be found as,

$$1.2 \geq \hat{r}_{ayw} \geq 0.8. \tag{21}$$

Moreover, in practice, it is found that, $L_y \geq L_w$. By introducing some margin for r_{lyw}, the range is found as,

$$2.5 \geq \hat{r}_{lyw} \geq 0.9. \tag{22}$$

However, it is to be noted that these ranges can be made wider or narrower to develop the required region.

5.4 Proposed ML Algorithm

Several ML-based algorithms have been developed for parameter identification. These algorithms are well developed in parameter identification process. However, these algorithms have some limitations and based on the limitations, one robust and effective algorithm is introduced. For example, the Gradient Descent Methods (GDMs) has the issue of sensitivity to the choice of learning rate and slow convergence (Al-Othman et al., 2022). Another algorithm named as Support Vector Machine (SVM) is an effective algorithm of parameter identification but requires significant time if the dataset is large (Al-Othman et al., 2022). The algorithm named Simulated Annealing (SA) is also can identify parameters correctly but has disadvantages such as slow convergence, sensitiveness to the cooling schedule, difficulty in setting the appropriate acceptance probability (Jiao et al., 2020). The PSO algorithm is widely used om parameter identification but its performance largely depends on the local optima (Cortez et al., 2022).

Addressing these issues, the Extreme Gradient Boosting (XGBoost) method with Five-fold Cross Validation is employed to identify the parameters (T. Chen & Guestrin, 2016; Friedman, 2001; Long et al., 2023). The method is renowned for its accuracy, robustness, and fast response (Shi et al., 2021). It is also effective in case of large dataset handling (Tarwidi et al., 2023). The XGBoost method has already been used in different power systems based applications such as load forecasting (Deng et al., 2022), voltage/var optimization (B. Zhang et al., 2024), and transient stability analysis (N. Li et al., 2020).The flowchart of the optimization algorithm is shown in Figure 8(a) and (b).

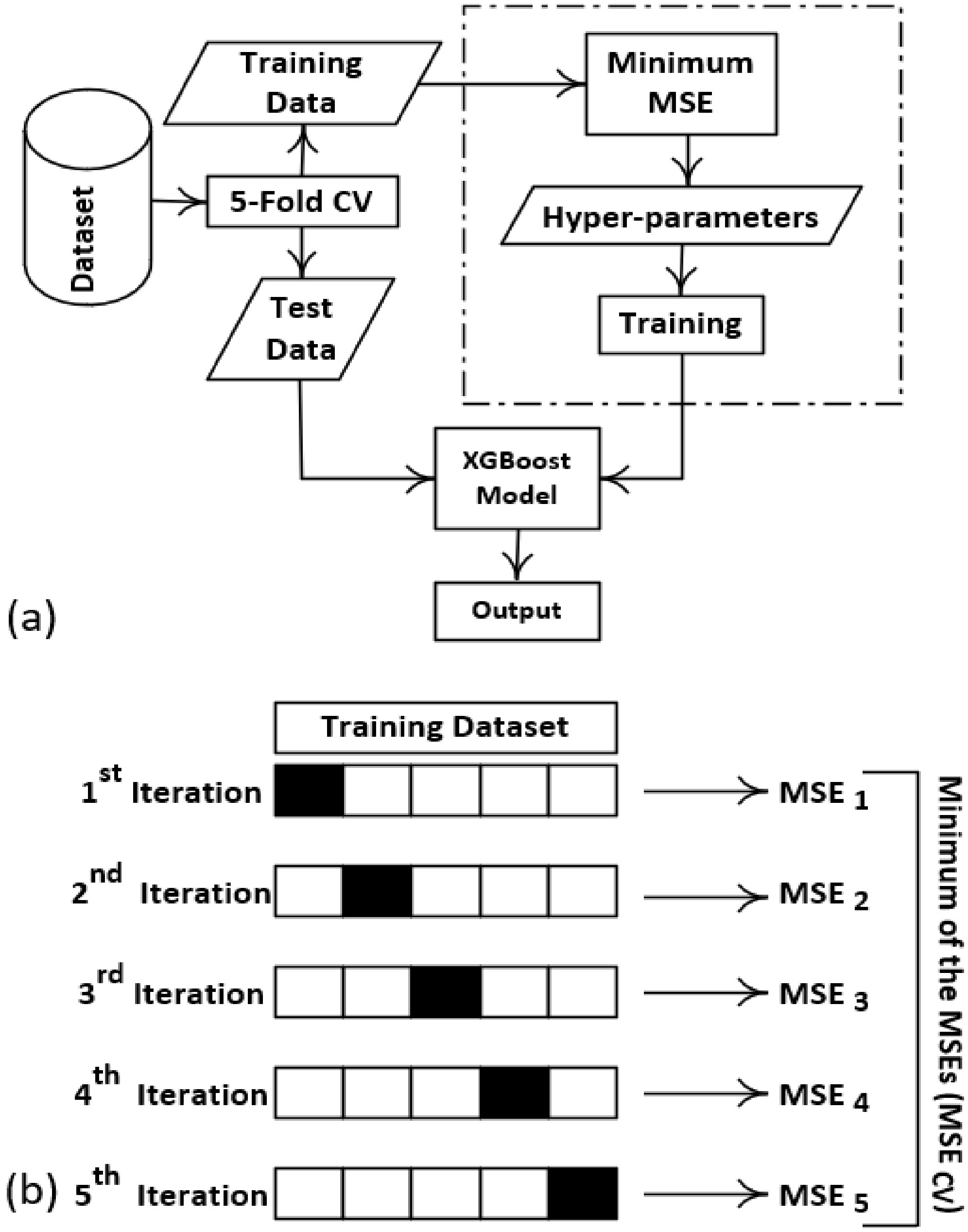

Figure 8. (a): The proposed XGBoost Model, (b) Five-fold Cross Validation.

(M. Chen et al., 2019; Xue & Wu, 2020; N. Zhang et al., 2021),

In the optimization algorithm, at first, a dataset D is constructed and defined as

$$D = \{(x_i, y_i): x_i \in \mathbb{R}^m, y_i \in \mathbb{R}, \forall i = 1,2, \dots, n\} \tag{23}$$

where x_i is the input variable which is the RMS value of $\hat{\imath}$ and the harmonic components of the RMS currents, y_i is the objective value corresponding to x_i, $\mathbb{R}$ is the real numbers, n indicates the number of samples in the dataset, m is the number of parameters associated with samples. It is to be noted that x_i includes parameters $\hat{r}_{ayw}$ and $\hat{r}_{lyw}$. $\mathbb{R}$ is the real numbers. Moreover, $m = 2$ since two parameters are required. The XGBoost is formulated as (N. Zhang et al., 2021),

$$\hat{y}_i = \sum\nolimits_{k=1}^{t} f_k(x_i), f_k \in \boldsymbol{F} \tag{24}$$

where $\hat{y}_i$ indicates the predicted value of the model, t is the number of trees, f_k is the independent regression tree, $f_k(x_i)$ is the prediction score that the k-th tree gives to the i-th sample x_i, and $\boldsymbol{F}$ represents the set of decision functions. The model is trained by minimizing the following objective function,

$$Obj = \sum_{i=1}^{n} L(y_i, \hat{y}_i) + \sum_{k=1}^{t} R(f_k) \tag{25}$$

where L is the loss function, $\hat{y}_i$ and the objective value y_i, R is the penalty term to avoid the overfitting issue. R is defined as (N. Zhang et al., 2021),

$$R(f_k) = \gamma T + \frac{1}{2}\lambda\left|\left|w\right|\right|^2 \tag{26}$$

where γ indicates parameter of regularization, λ is the regularization weight parameter, T denotes the number of leaf nodes, and w is the score on each leaf. λ ensures that the weights on the leaf nodes are not extensively large while γ controls the splitting of nodes. A new tree is created by XGBoost in each iteration along the development of the classification tree. The recursive construction process of the XGBoost model is as follows (N. Zhang et al., 2021),

$$\begin{cases} \hat{y}_i(0) = 0 \\ \hat{y}_i(1) = f_1(x_i) = \hat{y}_i(0) + f_1(x_i) \\ \hat{y}_i(2) = f_1(x_i) + f_2(x_i) \\ \vdots \\ \hat{y}_i(t) = \hat{y}_i(t-1) + f_t(x_i) \end{cases}, \tag{27}$$

Applying the last equation of (27) in (25) yields

$$Obj(t) = \sum_{i=1}^{n} L\big(y_i, \hat{y}_i(t-1) + f_t(x_i)\big) + R(f_t) + O. \tag{28}$$

where O is a constant number resulting from the sum of $R(f_1) + R(f_1) + \cdots + R(f_{t-1})$.

Using the second order Taylor expansion to (28),

$$Obj(t) \approx \sum_{i=1}^{n} \left(g_i f_t(x_i) + \frac{1}{2} h_i f_t^2(x_i)\right) + R(f_t) \tag{29}$$

where $g_i = \partial L\big(y_i, \hat{y}_i(t-1)\big)/\hat{y}_i(t-1)$ and $h_i = \partial^2 L\big(y_i, \hat{y}_i(t-1)\big)/\partial\big(\hat{y}_i(t-1)\big)^2$ are the first and second-order gradients of the loss function L, respectively. Applying (26) to (29),

$$\begin{gathered} Obj(t) = \sum_{i=1}^{n} \left(g_i f_t(x_i) + \frac{1}{2} h_i f_t^2(x_i)\right) + \\ \gamma T + \frac{1}{2}\lambda \sum_{j=1}^{T} w_j^2 = \\ \sum_{j=1}^{T} \left(\left(\sum_{i \in I_j} g_i \right) w_j + \frac{1}{2} \left(\sum_{i \in I_j} h_i + \lambda \right) w_j^2 \right) + \gamma T \end{gathered} \tag{30}$$

where $I_j = \{i : q(x_i) = j\}$ is the instance set of the j-th leaf node, and $q(x_i)$ represents the input for a fixed tree structure q. As set, $G_j = \sum_{i \in I_j} g_i$ and $H_j = \sum_{i \in I_j} h_i$, for a fixed tree structure of q, the optimal weight w_j^* of the leaf j is,

$$\begin{cases} w_j^* = -\dfrac{G_j}{H_j + \lambda} \\ Obj^* = -\dfrac{1}{2} \displaystyle\sum_{j=1}^{T} \dfrac{G_j^2}{H_j + \lambda} + \lambda T \end{cases} \tag{31}$$

where G_j and H_j respectively represent the quality of the tree and structure. A greedy algorithm is used to add branches iteratively. The gain is found after counting the feasible segmentation points while also choosing the maximum gain partition as (M. Chen et al., 2019),

$$G = \frac{1}{2}\left(\underbrace{\frac{\left(\sum_{i\in I_L} g_i\right)^2}{\sum_{i\in I_L} h_i + \lambda}}_{1^{st}\,Term} + \underbrace{\frac{\left(\sum_{i\in I_R} g_i\right)^2}{\sum_{i\in I_R} h_i + \lambda}}_{2^{nd}\,Term} - \underbrace{\frac{\left(\sum_{i\in I} g_i\right)^2}{\sum_{i\in I} h_i + \lambda}}_{3^{rd}\,Term}\right) - \gamma \tag{32}$$

where I_L and I_R are the instance set of left and right nodes after the split, respectively. As many simple trees are produced to score a leaf node during the splitting, the first, second, and third term of (32) respectively represents the score on the left, right, and original leaves. When the optimal splitting point is found by (32), the classification model is established.

As the dataset is constructed, the model requires hyper-parameters to be optimized to avoid overfitting. The selection of correct hyper-parameters results in higher model accuracy. In this project, five-fold cross validation is used for this process which is based on (S. Zhang et al., 2018). In this process, the training data is divided into five parts. As shown in Figure. 7 (b). At first iteration, the first part of the data is employed for testing. Meanwhile, the other four parts are used for training purposes (Picard & Cook, 1984). The Mean Square Error (MSE) found during the first iteration is calculated as (Long et al., 2023),

$$MSE(y_i, \hat{y}_i) = \frac{1}{N_{samples}} \sum_{i=0}^{N_{samples}-1} (y_i - \hat{y}_i)^2 \tag{33}$$

where $N_{samples}$ is the number of samples in the training set. The resultant MSE in the first iteration (MSE_1) is recorded and used for later comparison. Then, in the second iteration, the second part of the data is used to test the model while the other four parts are utilized for training purposes. Until all the fifth parts are covered, this process is continued. Then, to accomplish the MSE cross validation, the resultant MSE_1, MSE_2, …, MSE_5 are compared and the smallest one is selected as MSE_{CV}, as shown in Figure. 7(b) and found as,

$$MSE_{CV} = \min\,(MSE_1, MSE_2, \dots, MSE_5). \tag{34}$$

As the hyper-parameters which are related to MSE_{CV} used as the optimized ones in the XGBoost model, the cross-validation makes the selection of hyper-parameters effective and correct. The learning rate sets the step size of the model, max_depth indicates the maximum depth of the trees, colsample_bytree selects the fraction of features, subsample determines the fraction of observation, and n_estimators control the number of trees. All these hyper-parameters together prevent the overfitting issue.

CHAPTER 6

IDENTIFICATION OF THE ASPECT RATIOS AND RESULTS

As the XGBoost model is trained, the RMS value of i^{true} and its harmonic contents are provided to the algorithm, the core aspect ratios are identified. To prove the accuracy of the approach, three three-limb transformers of different configuration, frequencies, power, and voltage rating are simulated. In this chapter, one illustrative test case is provided along with other test cases to validate the accuracy of the proposed approach. In Table 4, the information regarding the transformers is provided in detail. The test system for identifying the aspect ratios is shown in Figure 9. The saturation curves of the transformers are shown in Figure. 10. MATLAB/Simscape is used for the simulation of transformer models. The second and fourth harmonics are also observed to ensure that voltages and currents both reach the steady-state situation. The measurements are taken and recorded when both the second and fourth harmonics reach zero. After that, the RMS value of $\hat{\imath}$ and its harmonic contents are found as harmonic phasors.

Table 4. Specification of The Transformers Used in The Test Cases

-	Nameplate Information		Core Dimensions and Ratios (A [m^2] and L [m])	
Tran-1 50 Hz (W. G. Enright, 1996)	Winding Config.	Delta-Star	$A_y = 0.5635$	$r_{ayw} = 1.01$
	Power	105 MVA	$A_w = 0.5555$	
	Primary Voltage	13.8 kV	$L_y = 4.000$	$r_{lyw} = 2.07$
	Secondary Voltage	220 kV	$L_w = 1.932$	
Tran-2 50 Hz (W. Enright et al., 1997)	Winding Config.	Star-Star	$A_y = 0.0122$	$r_{ayw} = 1.00$
	Power	40 kVA	$A_w = 0.0122$	

	Primary Voltage	240 V	$L_y = 0.180$	$r_{lyw} = 1.03$
	Secondary Voltage	70 V	$L_w = 0.175$	
Tran-3 60 Hz (Shafieipour et al., 2020)	Winding Config.	Star-Delta	$A_y = 0.31004$	$r_{ayw} = 1.00$
	Power	83.3 MVA	$A_w = 0.31004$	
	Primary Voltage	13.8 kV	$L_y = 2.37$	$r_{lyw} = 1.04$
	Secondary Voltage	6.972 kV	$L_w = 2.276$	

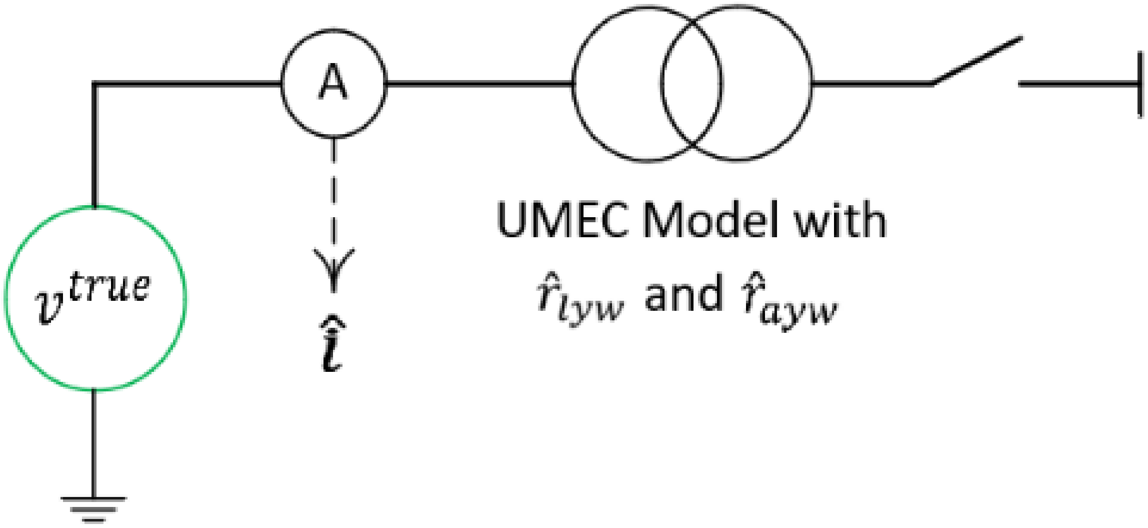

Figure 9. Test setup of the system.

To develop the dataset, the boundaries are set based on (21) and (22). The increment is set as 0.005 that resulted in generation of 25,600 instances. The simulation is completed by using a workstation computer with an i7 CPU supporting 24 cores and 80GB RAM. As the number of instances of simulation is high, parallel computation abilities of the MATLAB is utilized where 24 simulations ran at the same time by establishing 24 independent workers. Using the formulation of the UMEC explained earlier, each of the dataset are established.

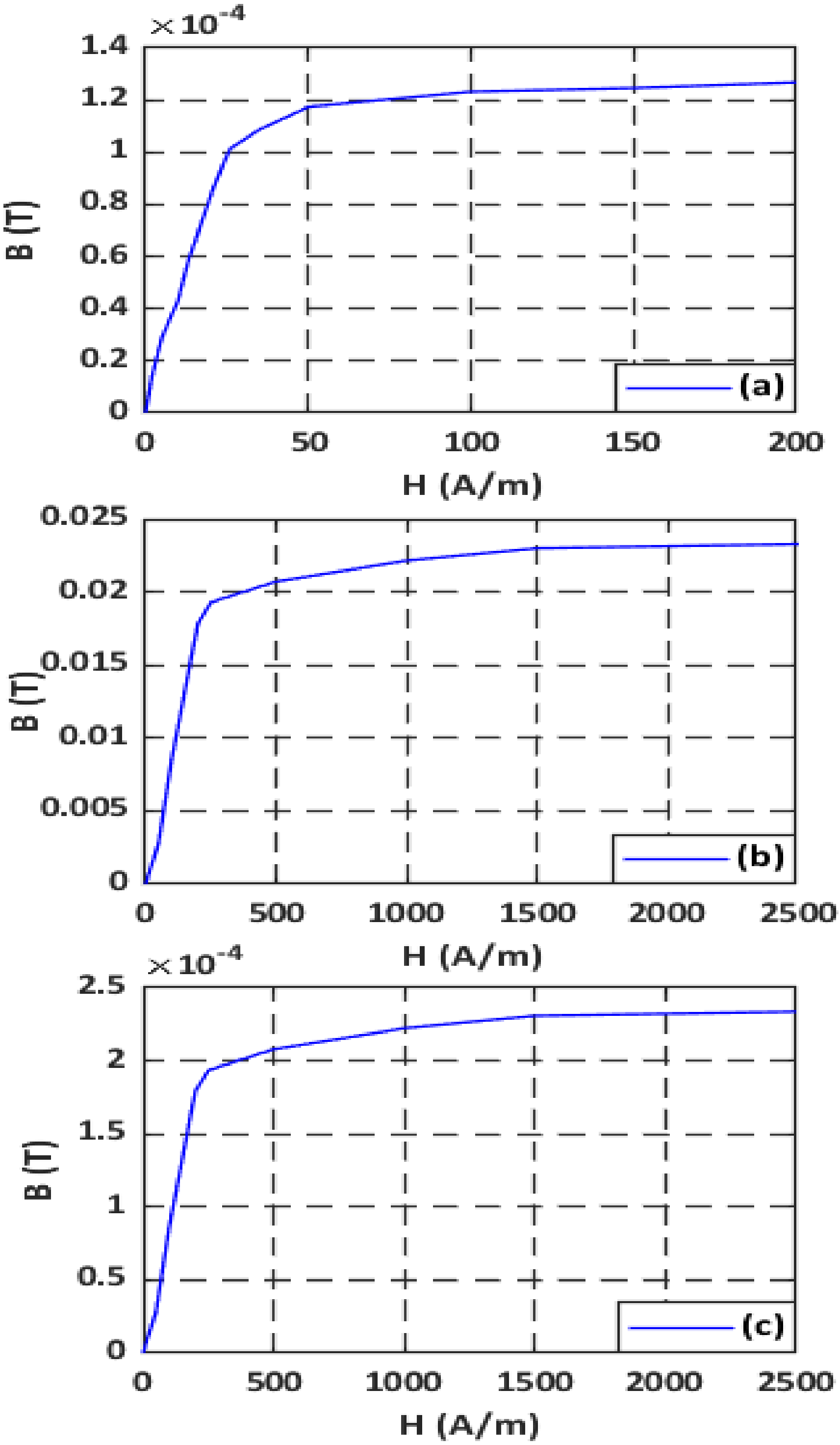

Figure 10. (a): Saturation curve for Tran-1 from (W. G. Enright, 1996),

(b): Saturation curve for Tran-2 from (Chaalani et al., 2023), (c): Saturation curve for Tran-3 from (Chaalani et al., 2023).

An illustrative test case is shown in the next section that explains the process and performance of the proposed method.

6.1 Illustrative Test Case

The illustrative test case uses information of the Tran-1 from Table 4. The primary side of the transformer (LV) is energized while the secondary side of the transformer (HV) side the kept open as shown in Figure 9. When the inrush current disappears or no even-harmonic exists, the measurements are taken. However, the odd harmonics may still be present as the transformer core gets saturated during the no-load situation (McLyman, 2004). The harmonic magnitude decreases with the increasing harmonic order. Hence, the harmonics of orders larger than nine (9) is disregarded in this test. Table 5 represents the RMS value of some $\hat{\imath}$'s and their harmonics in the phasor form (i.e., peak and angle) resulting from different aspect ratios ($\hat{r}_{lyw}$ and $\hat{r}_{ayw}$) which are simulated. Moreover, Table 5 represents each instance x_i which includes the calculated current and y_i which includes aspect ratios. The hyper-parameters found from the five-fold cross validation are shown in Table 6.

Figures 11, 12, and 13 illustrate the differences in transformer currents for different aspect ratios. The true aspect ratios of Tran-1 are $r_{lyw}^{true} = 2.07$ and $r_{ayw}^{true} = 1.01$. The figures depict phases a, b, and c currents when $\hat{r}_{lyw}$ and $\hat{r}_{ayw}$ are slightly different from the trye aspect ratios. In this table, No. 3 indicates the currents for the true ratios.

Table 5. Transformer Currents and Their Harmonic Contents for Different Core Aspect Ratios

No.	y_i		x_i					
	Core Aspect Ratios		LV-side Phase-A Current			…	LV-side Phase-C Current	
	$\hat{r}_{lyw}$	$\hat{r}_{ayw}$	$\hat{\imath}$ (RMS)	1st Har[†] $peak\ \angle$Ang[‡]	3rd Har $peak\angle$Ang	…	7th Har $peak\angle$Ang	9th Har $peak\angle$Ang
1	2.05	1.01	25.6294	35.3613 $\angle -99.44$	0.1064 $\angle -89.42$	…	0.1839 $\angle 43.40$	0.0351 $\angle 91.64$
2	2.06	1.01	25.7078	35.4725 $\angle -99.47$	0.1069 $\angle -89.42$	…	0.1844 $\angle 43.42$	0.0353 $\angle 91.63$
3	2.07	1.01	25.7889	35.5837 $\angle -99.50$	0.1074 $\angle -89.42$	…	0.1850 $\angle 43.45$	0.0354 $\angle 91.64$
4	2.07	1.00	26.1322	36.0634 $\angle -99.63$	0.1074 $\angle -89.41$	…	0.1850 $\angle 43.46$	0.0354 $\angle 91.65$
5	2.07	0.99	26.4866	36.5578 $\angle -99.75$	0.1075 $\angle -89.40$	…	0.1851 $\angle 43.48$	0.0355 $\angle 91.68$

[†] Har stands for Harmonic.
[‡] Ang indicates angle in degrees.

Table 6. Optimized Hyper-parameters for the XGBoost Model

Parameter Name	Value
learning rate	0.01
subsample	0.8
max_depth	3
n_estimators	1000
colsample_bytree	0.8

Figure 11(a) shows Phase-a true currents (i_a^{true}) and the calculated current ($\hat{\imath}_a$) with $\hat{r}_{lyw} = 2.06$ where true value is $\hat{r}_{lyw} = 2.06$, but $r_{ayw}^{true} = 1.01$. The error defined as $Error = i^{true} - \hat{\imath}_a$ which results from the deviation in $\hat{r}_{lyw}$ is shown in Figure 11(d). Again, while keeping the $\hat{r}_{lyw} = 2.07$, but changing $\hat{r}_{ayw} = 1.00$, the same comparison is shown in Figure 11(b) while the error is shown in Figure 11(e).

Although the true aspect ratios are unknown in practice, a sample in the dataset was made by utilizing the true aspect ratios which results in the best-calculated current $\hat{\imath}_a^*$, as shown in Figure 11(c), and its resultant error is equal to zero, as found in Figure 11(f). However, it is to be noted that when the feasible aspect ratios include the exact true values (i.e., $\hat{r}_{lyw} = r_{lyw}^{true}$ and $\hat{r}_{ayw} = r_{ayw}^{true}$), zero error can be achieved which is only in the ideal situation. Moreover, there are no noises and inaccuracies in the measured v^{true} and i^{true}.

Figures 12 and 13 provide the same analysis as described in Figure 11. Figure 12(a), (b), and (c) show the calculated currents with different ratios along with the true value of Phase-b current. In Figure 12(a) and (b), one ratio is deviated while the other is kept constant. Terrors from true and calculated currents are shown in Figure 12(d) and (e). However, the true current and calculated current with the true ratios is shown in Figure 11(c). Since both the curves are identical, the result is zero as shown in Figure 12(f).

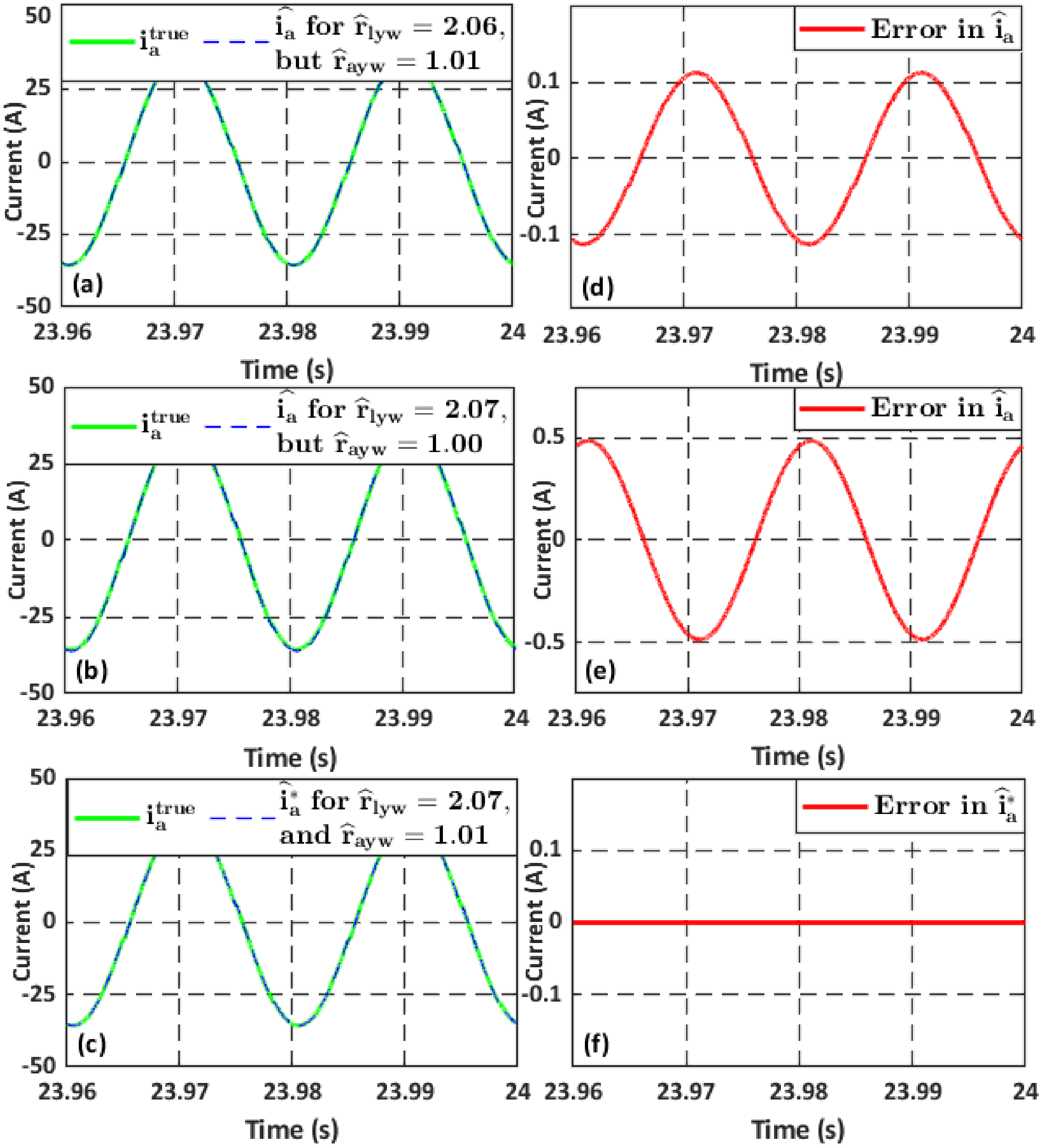

Figure 11. (a), (b) and (c) are Phase-a's true and calculated currents of Tran-1.

(d), (e), and (f) are the errors corresponding to the true and

calculated currents of (a), (b), and (c) respectively.

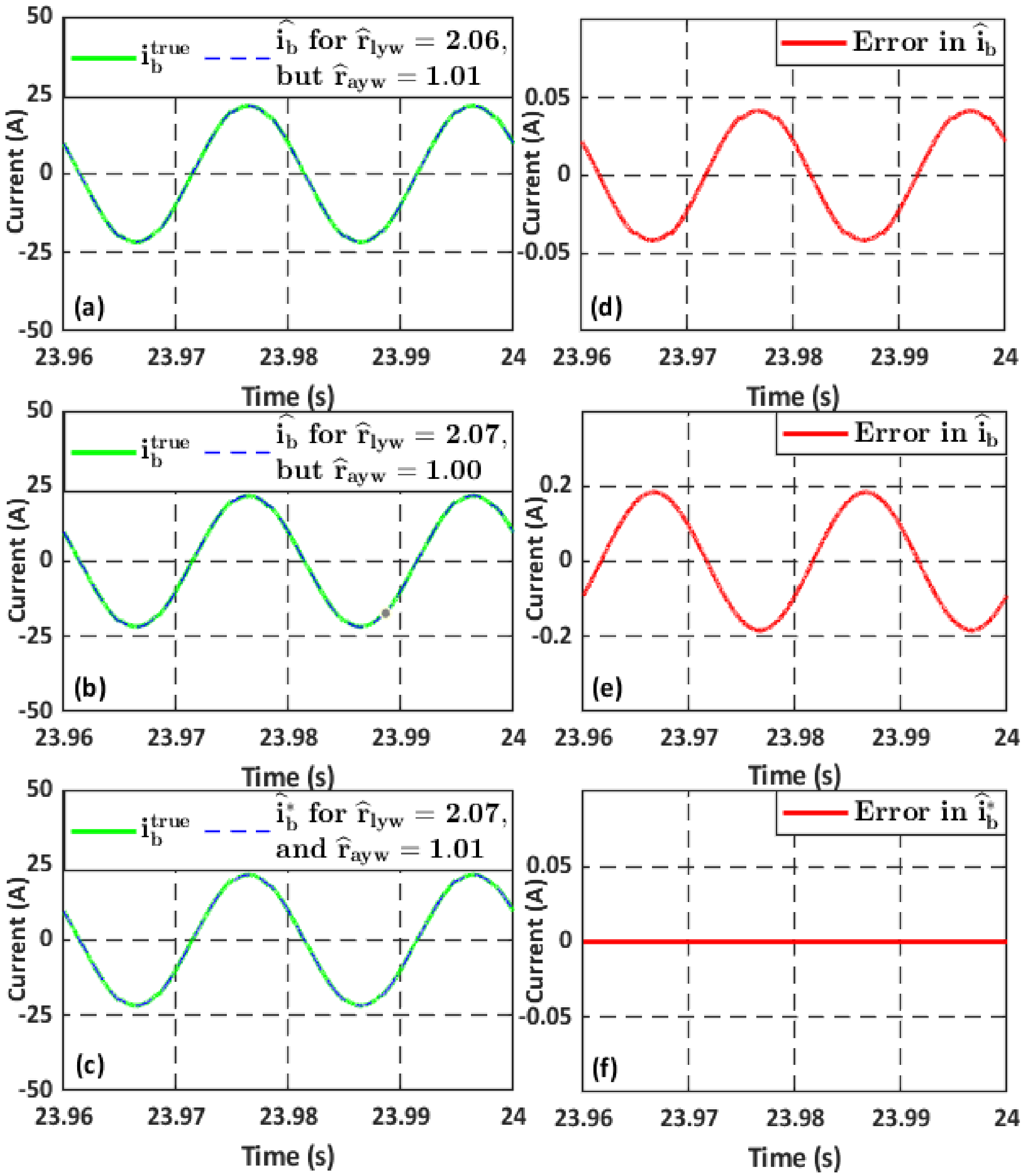

Figure 12. (a), (b) and (c) are Phase-b's true and calculated currents of Tran-1. (d), (e), and (f) are the errors corresponding to the true and calculated currents of (a), (b), and (c) respectively.

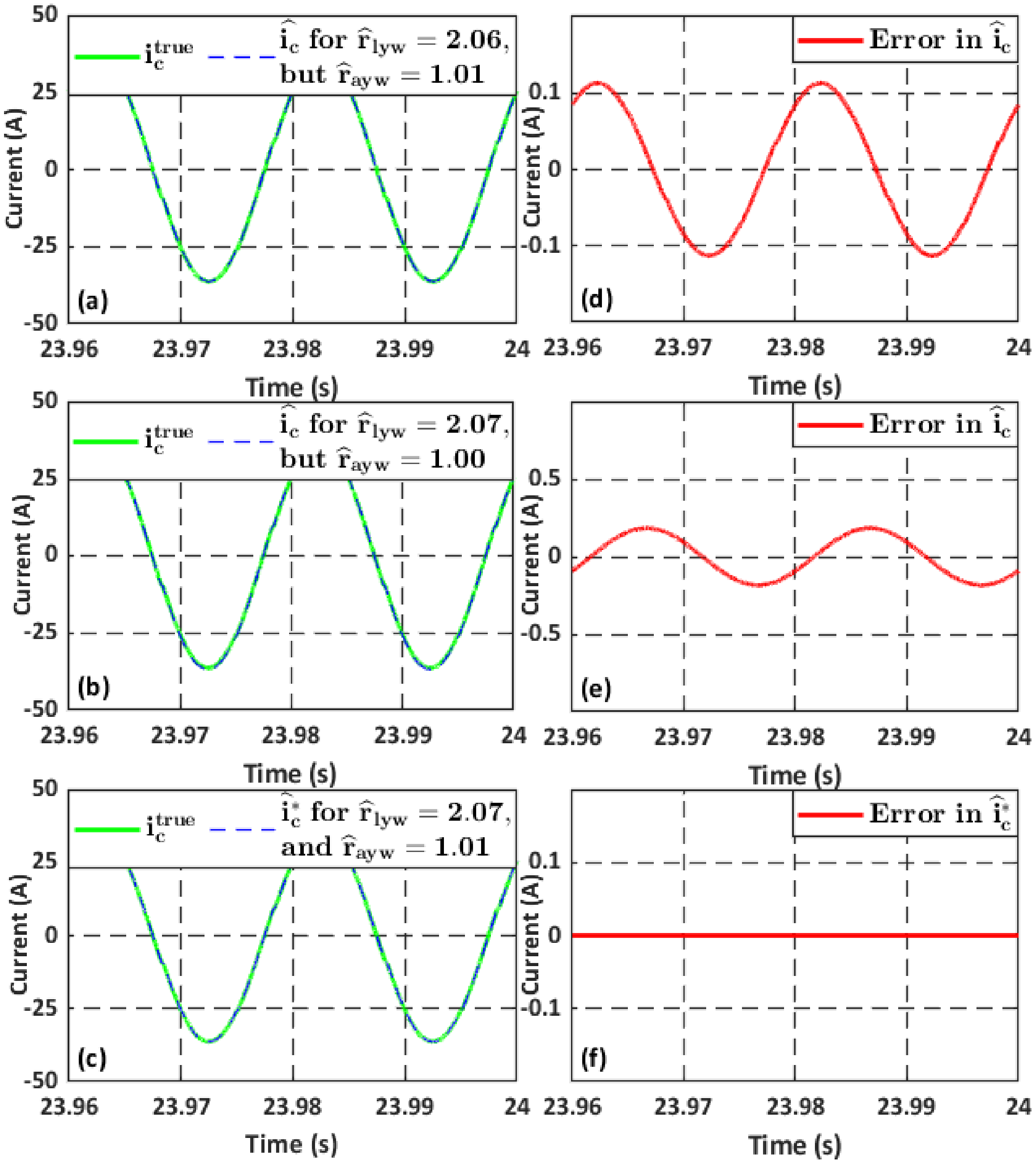

Figure 13. (a), (b) and (c) are Phase-c's true and calculated currents of Tran-1. (d), (e), and (f) are the errors corresponding to the true and calculated currents of (a), (b), and (c) respectively.

The true value of Phase-c current (i_c^{true}) and the calculated currents ($\hat{\imath}_c$) for different $\hat{r}_{lyw}$'s and $\hat{r}_{ayw}$'s are depicted in Figure 12(a), (b), and (c) which is similar to Figures 11 and 12. In Figure 13(a) and (b), one of the ratios is slightly different from the true ratio. The resulting errors are provided in Figure 13(d) and (e). Figure 13(c) depicts the calculated current with the true aspect ratio that leads to an ideal zero error, which is shown in Figure 13(f).

In addition to the figures, certain evaluation indicators are also found which evaluate the performance of the proposed method. These indicators are Mean Square Error (MSE), Root Mean Square Error (RMSE), Coefficient of determination (R^2) and Mean Absolute Error (MAE). These indicators are evaluated as (Long et al., 2023; Nguyen et al., 2021):

$$MSE(y_i, \hat{y}_i) = \frac{1}{N_{samples}} \sum_{i=1}^{N_{samples}} (y_i - \hat{y}_i)^2 \tag{35}$$

$$MSE(y_i, \hat{y}_i) = \sqrt{\frac{1}{N_{samples}} \sum_{i=1}^{N_{samples}} (y_i - \hat{y}_i)^2} \tag{36}$$

$$R^2(y_i, \hat{y}_i) = 1 - \frac{\sum_{i=1}^{N_{samples}} (y_i - \hat{y}_i)^2}{\sum_{i=1}^{N_{samples}} (y_i - \bar{y}_i)^2} \tag{37}$$

$$MAE(y_i, \hat{y}_i) = \frac{1}{N_{samples}} \sum_{i=1}^{N_{samples}} |y_i - \hat{y}_i|. \tag{38}$$

The variables of the parameters are described in (23) and (34). Table 7 shows the evaluation indicators found for $\hat{r}_{lyw} = 2.065$ and $\hat{r}_{ayw}$=1.005. Table 8 provides the evaluation indicators for the best instance calculated with r_{lyw}^{true} and r_{ayw}^{true}. By comparing the indicators in Table 7 and 8, it is found that the MSE, RMSE, and MAE in Table 7 are all larger than those in Table 8. This instance is predictable as these indicators are larger for instances other the best fit. It is to be noted that error indices are not absolutely zero and R^2

is not perfectly one in Table 8 because of some numerical errors associated with the numerical differential equation solvers as well as the nonlinearity of the core.

Table 7. True and Instance Core Aspect Ratios and Evaluation Indicators of the Tran-1

Aspect Ratios	True Ratios	Instance Ratios	MSE	$RMSE$	R^2	MAE
r_{lyw}	2.07	2.065	0.0098	0.0989	0.6367	0.0144
r_{ayw}	1.01	1.005				

Table 8. True and Identified Core Aspect Ratios and Evaluation Indicators of the Tran-1

Aspect Ratios	True Ratios	Identified Ratios	MSE	$RMSE$	R^2	MAE
r_{lyw}	2.07	2.07	9×10^{-5}	9.48×10^{-3}	0.9998	18.1×10^{-5}
r_{ayw}	1.01	1.01				

6.2 Other Test Cases

In this section, the test results for Tran-2 and Tran-3 are provided. However, in these transformers, the true ratios do not exist among the feasible ratios. To solve this issue, the boundaries of the feasible region are set as $1.201 \geq \hat{r}_{ayw} \geq 0.801$ and $2.501 \geq \hat{r}_{lyw} \geq 0.901$. Therefore, the increments of 0.005 do not generate an instance with the exact true values of aspect ratios.

Figures 14, 15, and 16 show the currents from Tran-2 as the core aspect ratios deviate from the true values. Phase-a's true and calculated currents are shown in Figure 14(a) and (b). Figure 14(c) and (d) are the respective errors corresponding to Figure 14(a) and (b). It is evident that the non-true ratios cause some errors in this case.

Figure 15(a) and (b) show the Phase-b's calculated and true currents. Their corresponding errors are depicted in Figure 15(c) and (d). Similarly, Figure 16(a) and (b) illustrate the

Phase-c's calculated and true currents while the errors are illustrated in Figure 16(c) and (d). From these figures, the calculated currents with for an instance with ratios unequal to the true values can be visualized.

It is evident from Figure 14(d), 15(d), and 16(d), the core nonlinearity causes some extra errors which are visualized from the jagged patterns for the error curves. Hence, the evaluation indicators are larger which indicates that the best fit will be imperfect. However, since the errors are negligible, the identified ratios are acceptable. Table 9 shows the identified ratios along with the evaluation indicators for Tran-2.

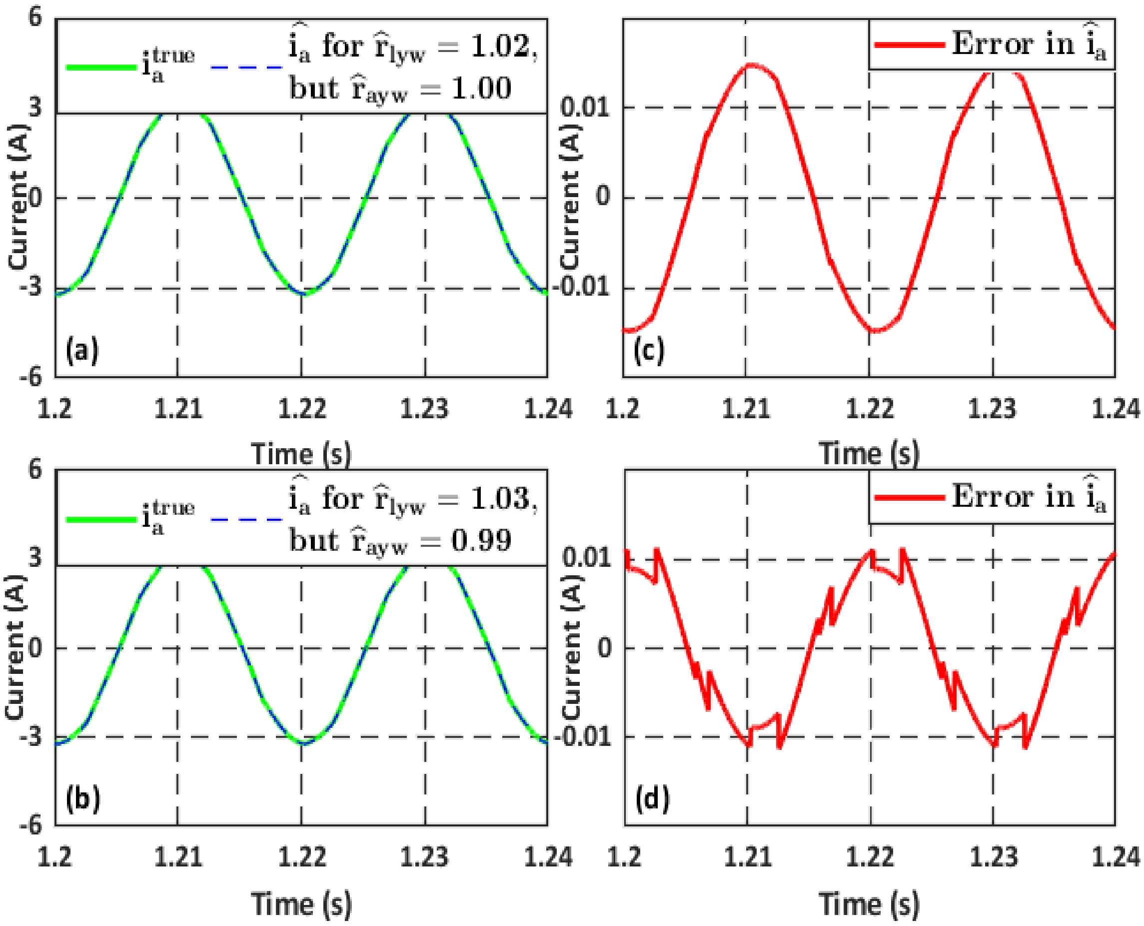

Figure 14. (a) and (b) are Phase-a's true and calculated currents of Tran-2.

(d) and (e) are the errors corresponding to the true and

calculated currents of (a) and (b) respectively.

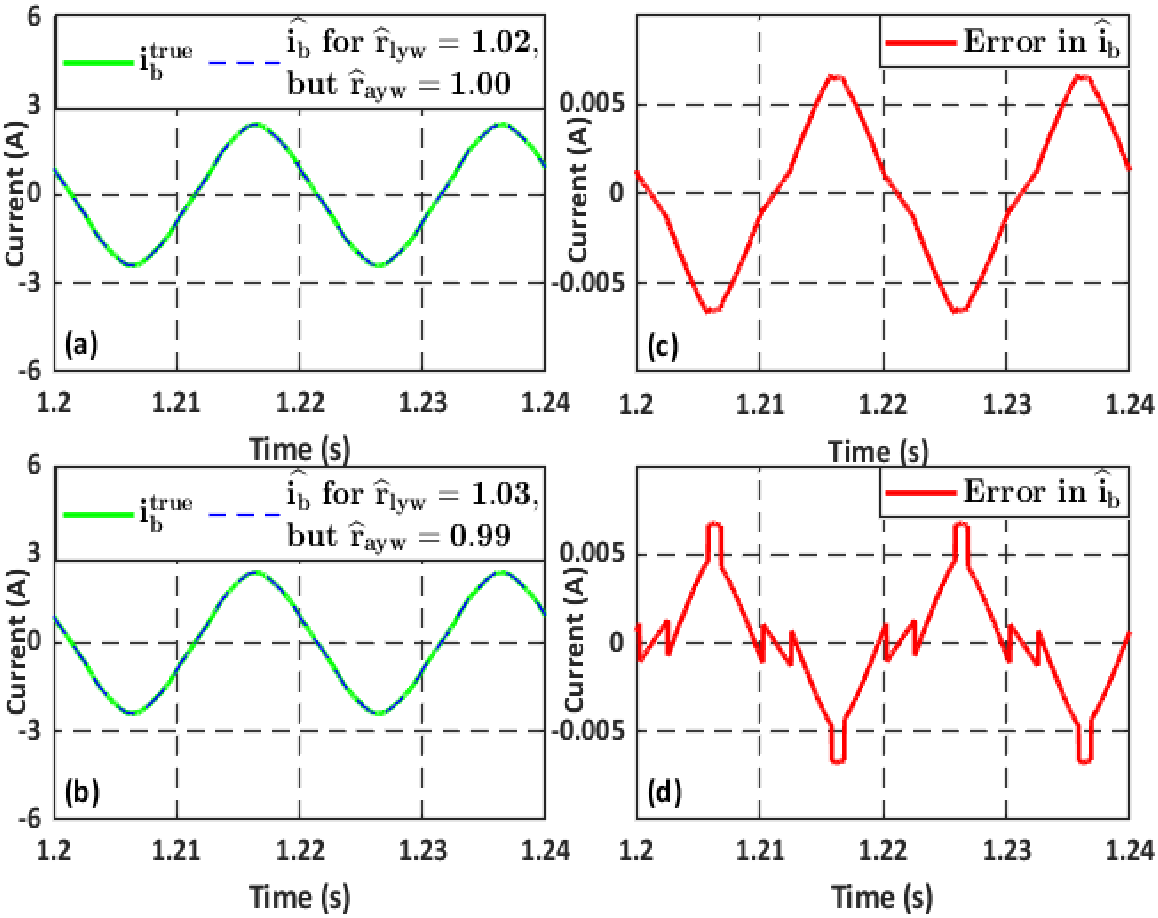

Figure 15. (a) and (b) are Phase-b's true and calculated currents of Tran-2. (d) and (e) are the errors corresponding to the true and calculated currents of (a) and (b) respectively.

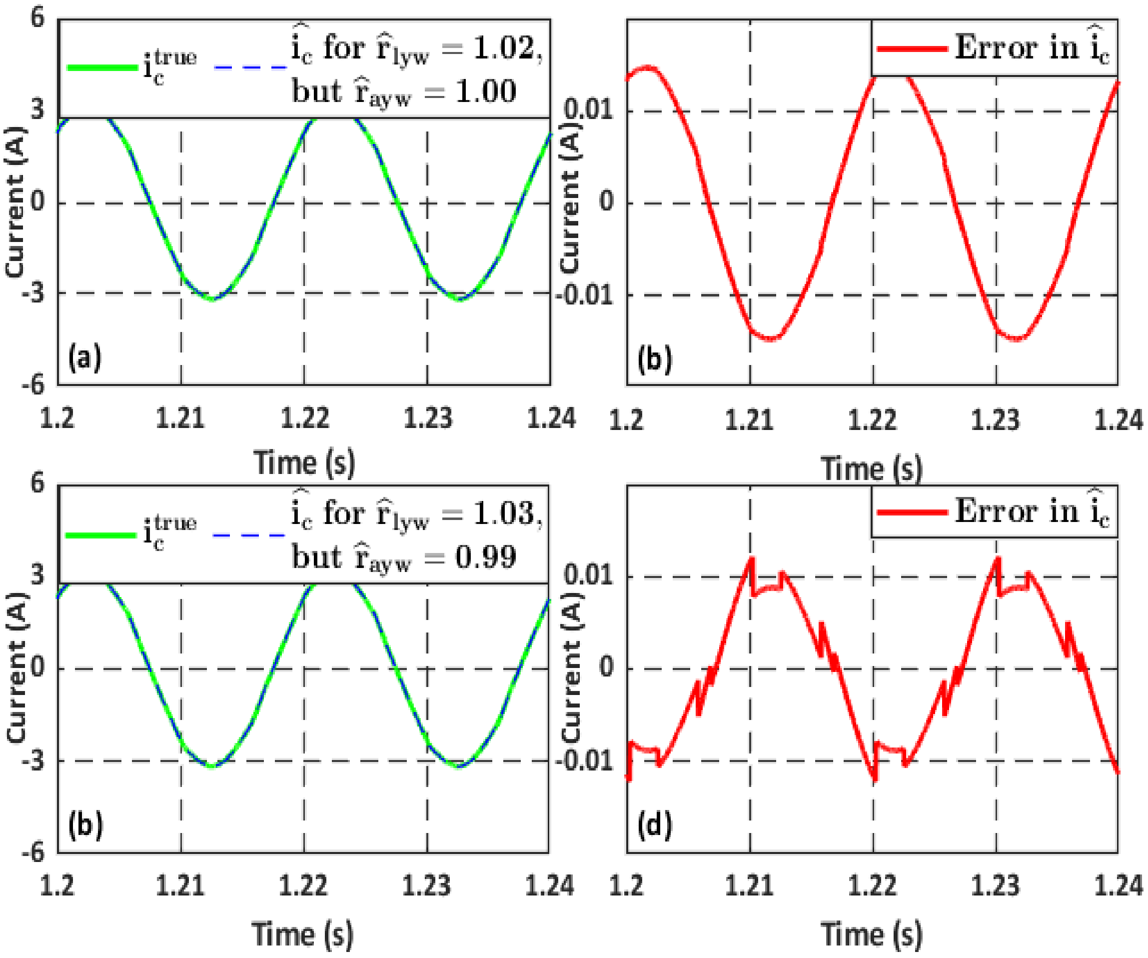

Figure 16. (a) and (b) are Phase-c's true and calculated currents of Tran-2.

(d) and (e) are the errors corresponding to the true and

calculated currents of (a) and (b) respectively.

Table 9. Aspect Ratios and Evaluation Indicators of the Tran-2

Aspect Ratios	True Ratios	Identified Ratios	MSE	$RMSE$	R^2	MAE
r_{lyw}	1.03	1.028	0.007	0.084	0.966	0.039
r_{ayw}	1.00	0.993				

The simulation is also performed for Tran-3. Figures 17, 18, and 19 illustrate the results for one instance. Figure 17(a) and (b) shows the Phase-a's true and calculated current for deviated ratios. The resultant errors are illustrated in Figure 17(c) and (d). Similar visualization can be found in Figure 18 and 19. The numerical inaccuracies that cause the spikes seen in the errors are that the solver deals with nonlinear saturation curves. However, those spikes are small in magnitude and can be neglected. The core aspect ratios are identified as $\hat{r}^*{}_{lyw} = 1.042$ and $\hat{r}^*{}_{ayw} = 1.003$. The proposed method identifies the which are very close to the true ratios. Table 10 shows the true and identified aspect ratios of the Tran-3 along with the evaluation indicators.

Table 10. Core Aspect Ratios and Evaluation Indicators of the Tran-3

Aspect Ratios	True Ratios	Identified Ratios	MSE	$RMSE$	R^2	MAE
r_{lyw}	1.04	1.042	0.005	0.071	0.985	0.0165
r_{ayw}	1.00	1.003				

From Table 9 and 10, it is evident that the proposed method is able to identify the aspect ratios of Tran-3 more precisely than Tran-2 since the error indicators in Tran-2 are smaller. Furthermore, R^2 in Trans-3 is larger than of the one in Tran-2. One reason of the numerical inaccuracies found in Tran-2 is the differential equation and iteration solution which deals with nonlinearities (T., 2018).

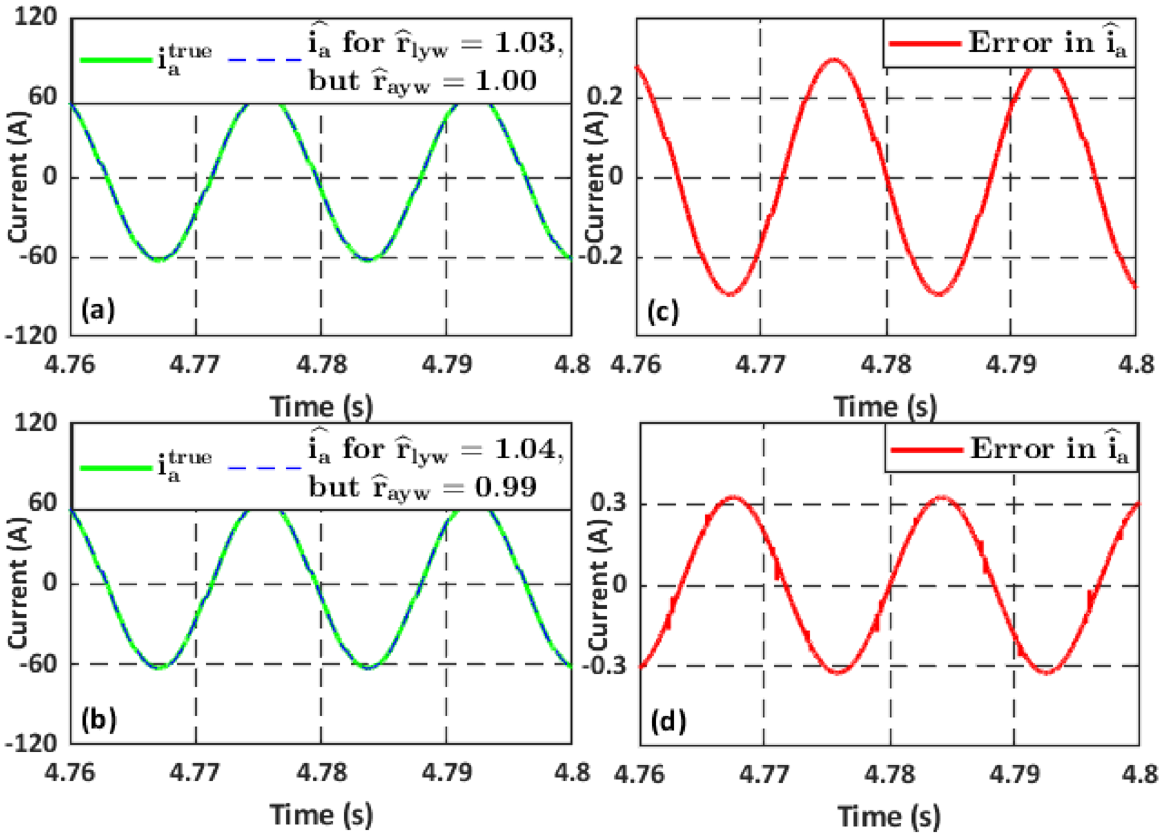

Figure 17. (a) and (b) are Phase-a's true and calculated currents of Tran-3.

(d) and (e) are the errors corresponding to the true and

calculated currents of (a) and (b) respectively.

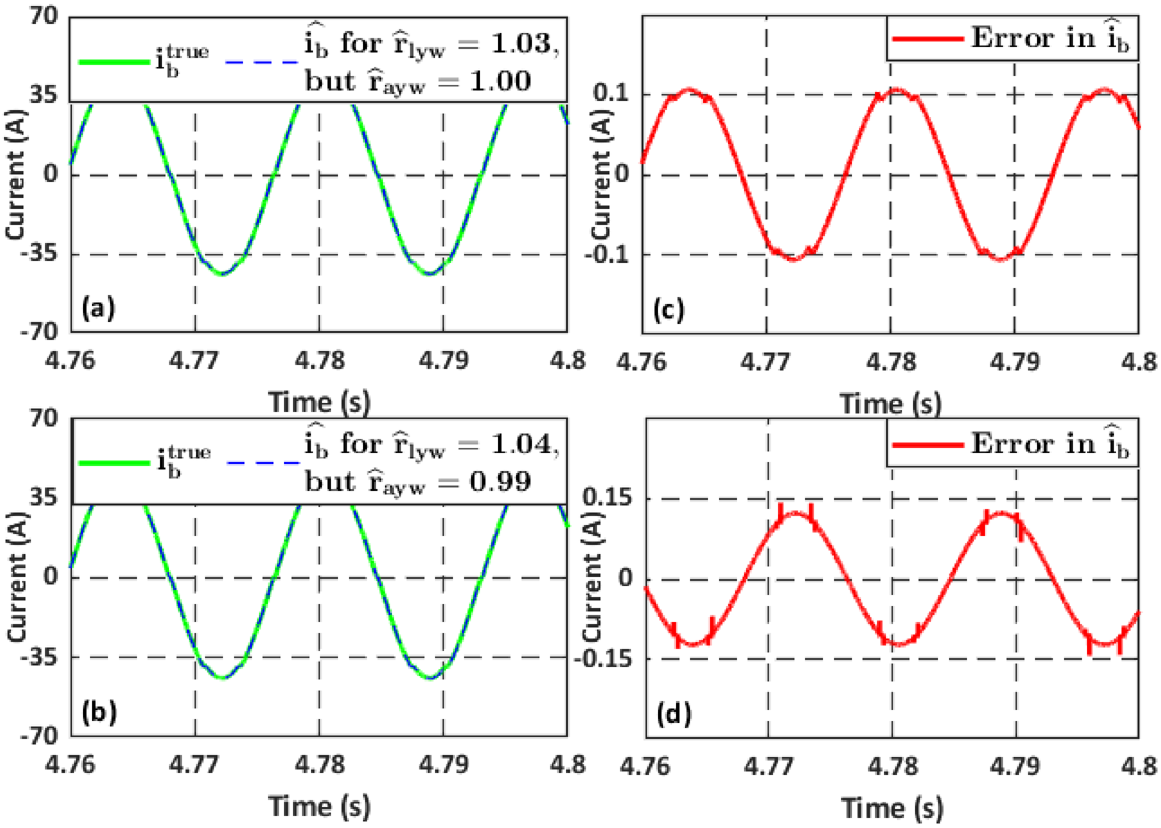

Figure 18. (a) and (b) are Phase-b's true and calculated currents of Tran-3.

(d) and (e) are the errors corresponding to the true and

calculated currents of (a) and (b) respectively.

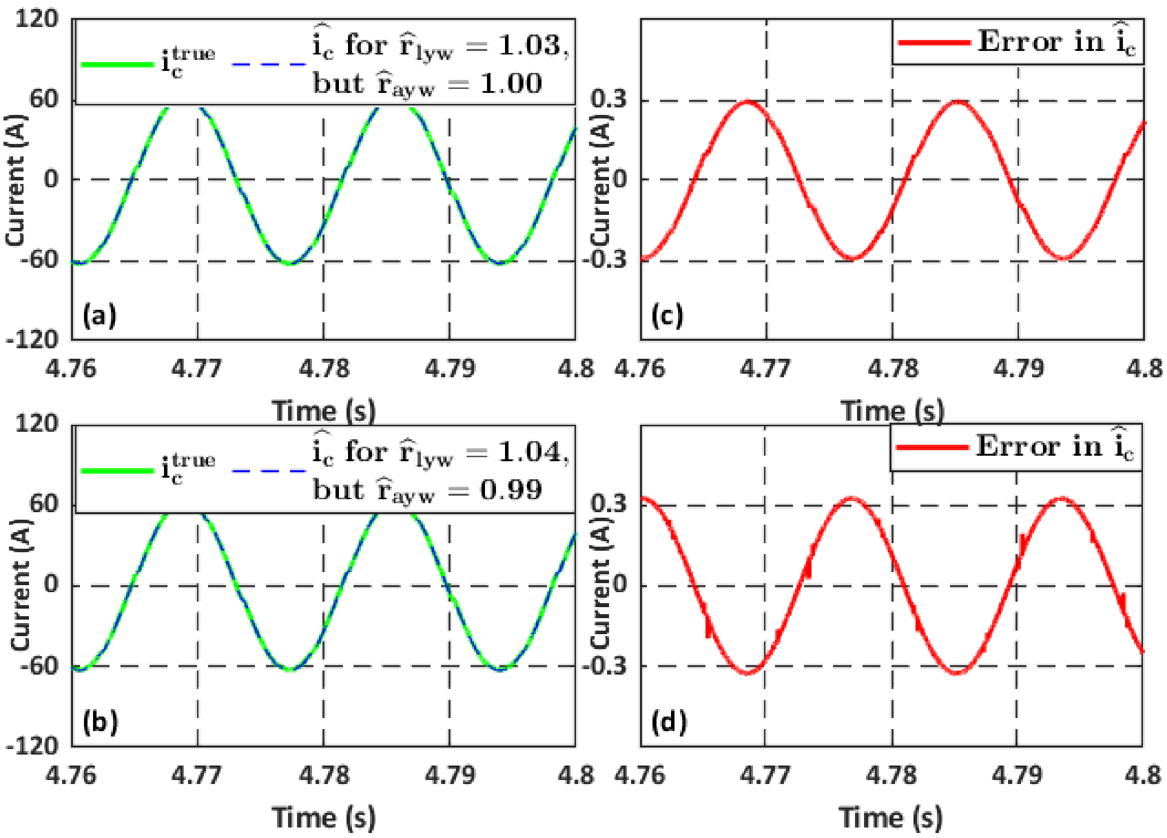

Figure 19. (a) and (b) are Phase-c's true and calculated currents of Tran-3. (d) and (e) are the errors corresponding to the true and calculated currents of (a) and (b) respectively.

To compare the proposed method with the other AI based methods, as described earlier, numerous attempts were taken using the GA and PSO. However, the algorithms did not provide any satisfactory results. The issue with GA and PSO has been explained in the earlier chapter.

CHAPTER 7

CONCLUSION AND FUTURE WORK

Power transformer transients such as inrush current have significant impact on the electric grids. Although several models are introduced to represent transformers, accurate transformer representation without certain core information is difficult. This leads to the introduction of the topological-based models which requires the core information of the transformers. Meanwhile, as the growth of Inverter Based Resources (IBRs) is rapid, accurate EMT-type studies cannot be avoided. However, these studies also require certain parameters such as core aspect ratios which are generally unavailable. In the light of this issue, the proposed algorithm is able to identify the core aspect ratios correctly.

The proposed algorithm does require any specific tests as routine tests are enough to generate the required dataset. Moreover, the phasor measurements can be used for dataset which is readily available and does not require any specific measuring device. Furthermore, the proposed modified UMEC model requires less computational time for dataset generation. Considering these advantages along with the accuracy evaluated for different transformers, the proposed algorithm can be considered successful.

The project proposed a ML-based XGBoost model with five-fold cross validation to identify the core aspect ratios which are considered as trade secret of the manufacturers. These parameters can be used for accurate core representation which is essential for the EMT-type studies. The proposed algorithm only uses non-load currents and their harmonic contents at steady-state situation to identify the aspect ratios. The performance of the proposed model is evaluated using three three-limb core-type transformers of different configurations, power, frequencies, and voltage ratings. For all the transformers, the proposed model is able to identify the aspect ratios while achieving a certain degree of accuracy. The robustness of the proposed method can be evaluated for the three-limb shell type transformers. Moreover, the method can be applied to the five-limb transformers in future. The test results along with the illustrative test case demonstrate the process and accuracy of the identification process. Based on the results, the project can be called successful.

REFERENCES

Abdelwanis, M. I., Abaza, A., El-Sehiemy, R. A., Ibrahim, M. N., & Rezk, H. (2020). Parameter estimation of electric power transformers using coyote optimization algorithm with experimental verification. *IEEE Access*, *8*, 50036–50044. https://doi.org/10.1109/ACCESS.2020.2978398

Al-Othman, A., Tawalbeh, M., Martis, R., Dhou, S., Orhan, M., Qasim, M., & Ghani Olabi, A. (2022). Artificial intelligence and numerical models in hybrid renewable energy systems with fuel cells: Advances and prospects. *Energy Conversion and Management*, *253*, 115154. https://doi.org/10.1016/j.enconman.2021.115154

Alvarez-Marino, C., De Leon, F., & Lopez-Fernandez, X. M. (2012). Equivalent circuit for the leakage inductance of multiwinding transformers: Unification of terminal and duality models. *IEEE Transactions on Power Delivery*, *27*(1), 353–361. https://doi.org/10.1109/TPWRD.2011.2173216

Ang, S. P. (2010). *Ferroresonance simulation studies of transmission systems*. The University of Manchester.

Azzouz, Z., Foggia, A., Pierrat, L., & Meunier, G. (1993). 3D finite element computation of the high frequency parameters of power transformer windings. *IEEE Transactions on Magnetics*, *29*(2), 1407–1410. https://doi.org/10.1109/20.250666

Bhowmick, D., Manna, M., & Chowdhury, S. K. (2018). Estimation of equivalent circuit parameters of transformer and induction motor from load data. *IEEE Transactions on Industry Applications*, *54*(3), 2784–2791. https://doi.org/10.1109/TIA.2018.2790378

Brandwajn, V., Donnel, H. W., & Dommel, I. I. (1982). Matrix representation of three-phase n-winding transformers for steady-state and transient studies. *IEEE Transactions on Power Apparatus and Systems*, *PAS-101*(6), 1369–1378. https://doi.org/10.1109/TPAS.1982.317184

Calasan, M., Jovanovic, A., Rubezic, V., Mujicic, D., & Deriszadeh, A. (2020). Notes on parameter estimation for single-phase transformer. *IEEE Transactions on Industry Applications*, *56*(4), 3710–3718. https://doi.org/10.1109/TIA.2020.2992667

Camelo-Daza, J. D., Betancourt-Alonso, D. N., Montoya, O. D., & Gómez-Vargas, E. (2024). Parameter estimation in single-phase transformers via the generalized normal distribution optimizer while considering voltage and current measurements. *Results in Engineering*, *21*, 101760. https://doi.org/10.1016/j.rineng.2024.101760

Chaalani, A., Hachi, D., Helifa, B., Lefkaier, I. K., & Feliachi, M. (2023). Determination of the normal magnetization curve in ferromagnetic steels by means of the eddy current approach using the brauer model. *Journal of Magnetism and Magnetic Materials*, *586*, 171147. https://doi.org/10.1016/j.jmmm.2023.171147

Chen, M., Liu, Q., Chen, S., Liu, Y., Zhang, C.-H., & Liu, R. (2019). XGBoost-based algorithm interpretation and application on post-fault transient stability status prediction of power system. *IEEE Access*, *7*, 13149–13158. https://doi.org/10.1109/ACCESS.2019.2893448

Chen, T., & Guestrin, C. (2016). XGBoost: A scalable tree boosting system. *22nd ACM SIGKDD International Conference on Knowledge Discovery and Data Mining*, 785–794. https://doi.org/10.1145/2939672.2939785

Cherry, E. C. (1949). The duality between interlinked electric and magnetic circuits and the formation of transformer equivalent circuits. *Proceedings of the Physical Society. Section B*, *62*(2), 101–111. https://doi.org/10.1088/0370-1301/62/2/303

Cho, S. D. (2002). *Parameter estimation for transformer modeling* [Ph.D. dissertation]. Michigan Technological University.

Cortez, R., Garrido, R., & Mezura-Montes, E. (2022). Spectral richness PSO algorithm for parameter identification of dynamical systems under non-ideal excitation conditions. *Applied Soft Computing*, *128*, 109490. https://doi.org/10.1016/j.asoc.2022.109490

Deng, X., Ye, A., Zhong, J., Xu, D., Yang, W., Song, Z., Zhang, Z., Guo, J., Wang, T., Tian, Y., Pan, H., Zhang, Z., Wang, H., Wu, C., Shao, J., & Chen, X. (2022). Bagging–XGBoost algorithm based extreme weather identification and short-term load forecasting model. *Energy Reports*, *8*, 8661–8674. https://doi.org/10.1016/j.egyr.2022.06.072

Dick, E. P., & Watson, W. (1981). Transformer models for transient studies based on field measurements. *IEEE Transactions on Power Apparatus and Systems*, *PAS-100*(1), 409–419. https://doi.org/10.1109/TPAS.1981.316870

Dirik, H., Gezegin, C., & Ozdemir, M. (2014). A novel parameter identification method for single-phase transformers by using real-time data. *IEEE Transactions on Power Delivery*, *29*(3), 1074–1082. https://doi.org/10.1109/TPWRD.2013.2284243

EMTP-RV. (n.d.). PGSTech, Montréal, Québec, CANADA. www.emtp.com

Enright, W. G. (1996). *Transformer models for electromagnetic transient studies with particular reference to HV dc transmission* [Ph.D. dissertation]. University of Canterbury.

Enright, W. G., Nayak, O., & Watson, N. R. (1999). Three-phase five-limb unified magnetic equivalent circuit transformer models for PSCAD V3. *Proc. Int. Conf. Power System Transients*, 462–467.

Enright, W., Nayak, O. B., Irwin, G. D., & Arrilaga, J. (1997). An electromagnetic transients model of multi-limb transformers using normalized core concept. *Proc. Int. Conf. Power System Transients*, 93–98.

Friedman, J. H. (2001). Greedy function approximation: A gradient boosting machine. *The Annals of Statistics*, *29*(5). https://doi.org/10.1214/aos/1013203451

Hamidi, R. J. (2023). Digital Twins for Power Transformers. *2023 IEEE Power & Energy Society General Meeting (PESGM)*, 1–5. https://doi.org/10.1109/PESGM52003.2023.10252549

IEEE Draft Guide to Describe the Occurrence and Mitigation of Switching Transients Induced by Transformers, Switching Device, and System Interaction. (2022). *IEEE PC57.142/D10, March 2022*, 1–70.

Illias, H. A., Mou, K. J., & Bakar, A. H. A. (2017). Estimation of transformer parameters from nameplate data by imperialist competitive and gravitational search algorithms. *Swarm and Evolutionary Computation*, *36*, 18–26. https://doi.org/10.1016/j.swevo.2017.03.003

Jazebi, S., & De Leon, F. (2015). Duality-based transformer model including eddy current effects in the windings. *IEEE Transactions on Power Delivery*, *30*(5), 2312–2320. https://doi.org/10.1109/TPWRD.2015.2424223

Jiao, Z., Zhang, J., Yao, P., Wan, L., & Ni, L. (2020). Service deployment of C4ISR based on genetic simulated annealing algorithm. *IEEE Access*, *8*, 65498–65512. https://doi.org/10.1109/ACCESS.2020.2981624

Jin, E. S., Liu, L. L., Bo, Z. Q., & Klimek, A. (2008). Parameter identification of the transformer winding based on least-squares method. *2008 IEEE Power and Energy Society General Meeting - Conversion and Delivery of Electrical Energy in the 21st Century*, 1–6. https://doi.org/10.1109/PES.2008.4596453

Kazemi, Z., Naseri, F., Yazdi, M., & Farjah, E. (2021). An EKF-SVM machine learning-based approach for fault detection and classification in three-phase power transformers. *IET Science, Measurement & Technology*, *15*(2), 130–142. https://doi.org/10.1049/smt2.12015

Li, N., Li, B., & Gao, L. (2020). Transient stability assessment of power system based on XGBoost and factorization machine. *IEEE Access*, *8*, 28403–28414. https://doi.org/10.1109/ACCESS.2020.2969446

Li, X., Wu, J., Ye, C., Wu, L., Zhang, D., & Ding, X. (2015). Transformer model with hysteresis characteristic for electromagnetic transients based on PSCAD/EMTDC. *2015 5th International Conference on Electric Utility Deregulation and Restructuring and Power Technologies (DRPT)*, 1689–1694. https://doi.org/10.1109/DRPT.2015.7432505

Long, X., Gu, X., Lu, C., Li, Z., Ma, Y., & Jian, Z. (2023). Prediction of the jump height of transmission lines after ice-shedding based on XGBoost and Bayesian optimization. *Cold Regions Science and Technology*, *213*, 103928. https://doi.org/10.1016/j.coldregions.2023.103928

Martinez, J. A., & Mork, B. A. (2005). Transformer modeling for low- and mid-frequency transients—A review. *IEEE Transactions on Power Delivery*, *20*(2), 1625–1632. https://doi.org/10.1109/TPWRD.2004.833884

Martinez, J. A., Walling, R., Mork, B. A., Martin-Arnedo, J., & Durbak, D. (2005). Parameter determination for modeling system transients—Part III: Transformers. *IEEE Transactions on Power Delivery*, *20*(3), 2051–2062. https://doi.org/10.1109/TPWRD.2005.848752

Martinez-Velasco, J. A. (2011). Equivalent circuit of transformers with control of voltage and phase angle. *Electric Power Systems Research*, *81*(7), 1349–1356. https://doi.org/10.1016/j.epsr.2011.01.019

McLyman, W. T. (2004). *Transformer and inductor design handbook* (3rd ed. revised and expanded). M. Dekker.

Mitchell, S. D., & Welsh, J. S. (2013). Initial parameter estimates and constraints to support gray box modeling of power transformers. *IEEE Transactions on Power Delivery*, *28*(4), 2411–2418. https://doi.org/10.1109/TPWRD.2013.2259266

Mork, B. A., Gonzalez, F., Ishchenko, D., Stuehm, D. L., & Mitra, J. (2007a). Hybrid transformer model for transient simulation—Part I: Development and parameters. *IEEE Transactions on Power Delivery*, *22*(1), 248–255. https://doi.org/10.1109/TPWRD.2006.883000

Mork, B. A., Gonzalez, F., Ishchenko, D., Stuehm, D. L., & Mitra, J. (2007b). Hybrid transformer model for transient simulation—Part II: Laboratory measurements and benchmarking. *IEEE Transactions on Power Delivery*, *22*(1), 256–262. https://doi.org/10.1109/TPWRD.2006.882999

Mossad, M. I., Azab, M., & Abu-Siada, A. (2014). Transformer parameters estimation from nameplate data using evolutionary programming techniques. *IEEE Transactions on Power Delivery*, *29*(5), 2118–2123. https://doi.org/10.1109/TPWRD.2014.2311153

Narang, A., & Brierley, R. H. (1994). Topology based magnetic model for steady-state and transient studies for three-phase core type transformers. *IEEE Transactions on Power Systems*, *9*(3), 1337–1349. https://doi.org/10.1109/59.336132

Nguyen, D. H., Hien Le, X., Heo, J.-Y., & Bae, D.-H. (2021). Development of an extreme gradient boosting model integrated with evolutionary algorithms for hourly water level prediction. *IEEE Access*, *9*, 125853–125867. https://doi.org/10.1109/ACCESS.2021.3111287

PENG, J. (2013). *Assessment of transformer energisation transients and their impacts on power systems*. The University of Manchester.

Picard, R. R., & Cook, R. D. (1984). Cross-validation of regression models. *Journal of the American Statistical Association*, *79*(387), 575–583. https://doi.org/10.1080/01621459.1984.10478083

Shafieipour, M., Garcia Alonso, J. C., Jayasinghe, R. P., & Gole, A. M. (2019). Principle of duality with normalized core concept for modeling multi-limb transformers. *Proc. Int. Conf. Power System Transients*, 1–6.

Shafieipour, M., Ziomek, W., Jayasinghe, R. P., Alonso, J. C. G., & Gole, A. M. (2020). Application of duality-based equivalent circuits for modeling multilimb transformers using alternative input parameters. *IEEE Access*, *8*, 153353–153363. https://doi.org/10.1109/ACCESS.2020.3018323

Shi, R., Xu, X., Li, J., & Li, Y. (2021). Prediction and analysis of train arrival delay based on XGBoost and Bayesian optimization. *Applied Soft Computing*, *109*, 107538. https://doi.org/10.1016/j.asoc.2021.107538

Srikanta Murthy, A., Azis, N., Jasni, J., Othman, M. L., Mohd Yousof, M. F., & Talib, M. A. (2020). Extraction of winding parameters for 33/11 kV, 30 MVA transformer based on finite element method for frequency response modelling. *PLOS ONE*, *15*(8), e0236409. https://doi.org/10.1371/journal.pone.0236409

Steinmetz, C. P., & Berg, E. J. (1900). *Theory and calculation of alternating current phenomena*. Electrical World and Engineer, inc.

T., S. (2018). *Numerical Analysis* (3rd ed.). Pearson.

Tarwidi, D., Pudjaprasetya, S. R., Adytia, D., & Apri, M. (2023). An optimized XGBoost-based machine learning method for predicting wave run-up on a sloping beach. *MethodsX*, *10*, 102119. https://doi.org/10.1016/j.mex.2023.102119

Thilagar, S. H., & Rao, G. S. (2002). Parameter estimation of three-winding transformers using genetic algorithm. *Engineering Applications of Artificial Intelligence*, *15*(5), 429–437. https://doi.org/10.1016/S0952-1976(02)00087-8

Xue, W., & Wu, T. (2020). Active learning-based XGBoost for cyber physical system against generic AC false data injection attacks. *IEEE Access*, *8*, 144575–144584. https://doi.org/10.1109/ACCESS.2020.3014644

Xusheng, C. (1996). A three-phase multi-legged transformer model in ATP using the directly-formed inverse inductance matrix. *IEEE Transactions on Power Delivery*, *11*(3), 1554–1562. https://doi.org/10.1109/61.517516

Yang, M., Kazemi, R., Jazebi, S., Deswal, D., & De Leon, F. (2018). Retrofitting the BCTRAN transformer model with nonlinear magnetizing branches for the accurate study of low-frequency deep saturating transients. *IEEE Transactions on Power Delivery*, *33*(5), 2344–2353. https://doi.org/10.1109/TPWRD.2018.2825252

Zhang, B., Gao, Y., Wang, L., & Li, T. (2024). BO-XGBoost-based voltage/var optimization for distribution network considering the LCOE of PV system. *IET Renewable Power Generation*, *18*(3), 502–514. https://doi.org/10.1049/rpg2.12868

Zhang, N., Qian, H., He, Y., Li, L., & Sun, C. (2021). A data-driven method for power system transient instability mode identification based on knowledge discovery and XGBoost algorithm. *IEEE Access*, *9*, 154172–154182. https://doi.org/10.1109/ACCESS.2021.3124051

Zhang, S., Wang, Y., Liu, M., & Bao, Z. (2018). Data-based line trip fault prediction in power systems using LSTM networks and SVM. *IEEE Access*, *6*, 7675–7686. https://doi.org/10.1109/ACCESS.2017.2785763